Mon. Not. R. Astron. Soc. **000**, 000–000 (0000) Printed 31 October 2021 (MN LATEX style file v2.2)

Multi-Epoch Observations of Extremely High-Velocity Emergent Broad Absorption

Jesse A. Rogerson,[1] ⋆ Patrick B. Hall,[1] Paola Rodríguez Hidalgo,[1,2] Patrik Pirkola,[1] William N. Brandt,[3,4,5] Nur Filiz Ak[6]

[1] *Department of Physics and Astronomy, York University, Toronto, ON M3J 1P3, Canada*
[2] *Department of Physics and Astronomy, Humbolt State University, Arcata, CA 95521, USA*
[3] *Department of Astronomy & Astrophysics, 525 Davey Lab, The Pennsylvania State University, University Park, PA 16802, USA*
[4] *Institute for Gravitation and the Cosmos, The Pennsylvania State University, University Park, PA 16802, USA*
[5] *Department of Physics, 104 Davey Lab, The Pennsylvania State University, University Park, PA 16802, USA*
[6] *Department of Astronomy and Space Sciences, Faculty of Sciences, Erciyes University, 38039 Kayseri, Turkey*

31 October 2021

ABSTRACT

We present the discovery of the highest velocity C IV broad absorption line to date in the z=2.47 quasar SDSS J023011.28+005913.6, hereafter J0230. In comparing the public DR7 and DR9 spectra of J0230, we discovered an emerging broad absorption trough outflowing at ∼60,000 km s^{-1}, which we refer to as trough A. In pursuing follow up observations of trough A, we discovered a second emergent C IV broad absorption trough outflowing at ∼40,000 km s^{-1}, namely trough B. In total, we collected seven spectral epochs of J0230 that demonstrate emergent and rapidly (∼10 days in the rest-frame) varying broad absorption. We investigate two possible scenarios that could cause these rapid changes: bulk motion and ionization variability. Given our multi-epoch data, we were able to rule out some simple models of bulk motion, but have proposed two more realistic models to explain the variability of both troughs. Trough A is likely an augmented 'crossing disk' scenario with the absorber moving at $10,000 < v$ (km s^{-1}) $< 18,000$. Trough B can be explained by a flow-tube feature travelling across the emitting region at $8,000 < v$ (km s^{-1}) $< 56,000$. If ionization variability is the cause for the changes observed, trough A's absorber has $n_e \geqslant 724$ cm^{-3} and is at $r_{equal} \geqslant 2.00$ kpc, or is at $r < 2.00$ kpc with no constraint on the density; trough B's absorber either has $n_e \geqslant 1540$ cm^{-3} and is at $r_{equal} \geqslant 1.37$ kpc, or is at $r < 1.37$ kpc with no constraint on the density.

Key words: quasars: general – quasars: absorption lines – quasars: emission lines – quasars: super massive black holes – quasars: individual: SDSS J0230+0059 accretion discs

1 INTRODUCTION

At least 23% of quasars exhibit blueshifted Broad Absorption Line (BAL) troughs at ultraviolet wavelengths (see discussions in Rogerson et al. 2011 and Allen et al. 2011), and the fraction increases if narrower (500-2000 km s^{-1}) 'mini-BAL' troughs are included (see Rodríguez Hidalgo et al. 2011 for a full discussion on mini-BAL quasars).[1] The disk-wind model of luminous Active Galactic Nuclei (AGN) characterizes BAL features as a result of material lifted off the accretion disk surrounding the central supermassive black hole (SMBH) and accelerated by radiation line driving to high outflow velocities that we observe as blueshifted absorption (e.g. Murray et al. 1995, Ostriker et al. 2010). Whatever their origin, quasar outflows provide insight into the physical and chemical properties of the central engine of quasars, and may also rep-

⋆ E-mail: rogerson@yorku.ca

[1] BAL quasars are, historically, defined as quasars that exhibit blueshifted absorption due to the C IV doublet at λλ 1548.203, 1550.770 Å that is at least 2000 km s^{-1} wide and can extend from 3000 km s^{-1} to 25000 km s^{-1}, where 0 km s^{-1} is at the systemic redshift of the quasar (Weymann et al. 1991) and positive velocities indicate motion toward the observer. Modifications to this definition have been proposed, e.g. Hall et al. (2002) and Trump et al. (2006). Herein, we consider absorption at any velocity to be a candidate BAL trough, and we report widths of confirmed troughs so that others may classify the troughs as they see fit.

resent a mechanism by which SMBHs provide feedback to their host galaxy (e.g., Moe et al. 2009, Arav et al. 2013, Leighly et al. 2014, Chamberlain et al. 2015).

Variability in the strength (i.e., the depth, width, or outflow velocity profile) of BALs is a well documented phenomenon (e.g., Gibson et al. 2008, Hall et al. 2011, Filiz Ak et al. 2013, He et al. 2015). Specifically, there have been recent studies documenting the disappearance of BAL troughs (e.g., Filiz Ak et al. 2012) as well as emergence in quasars that were not classified as having BALs previously (e.g., Rodríguez Hidalgo et al., in preparation, Hamann et al. 2008, Leighly et al. 2009).

The cause of BAL-trough variability is still largely debated in the literature, however, it is likely either due to transverse motion of absorbing clouds across our line of sight (e.g., Hall et al. 2011, Muzahid et al. 2015), or due to changes in the ionization of the absorbing gas (e.g., Hamann et al. 2008, Filiz Ak et al. 2013, Wang et al. 2015). Ultimately, it may be a complex mixture of these two scenarios. Full characterization of BAL variability events (either emergence, disappearance, or variability in general) would significantly increase our understanding of both the physics of the quasar's central engine and the interaction of the quasar with its host galaxy.

In this work we present the discovery of the highest velocity outflow discovered to date ($\sim$60,000 km s^{-1}) at ultraviolet wavelengths, in the quasar SDSS J023011.28+005913.6, hereafter J0230 (Schneider et al. 2007). The previous highest-velocity absorption identified at ultraviolet wavelengths in a BAL quasar was at 56,000 km s^{-1} in PG 2302+029 (Jannuzi et al. 1996), with the next highest being at 50,000 km s^{-1} in PG 0935+417 (Rodríguez Hidalgo et al. 2011).[2] Outflows at these extremely high velocities have been previously observed in X-rays (e.g., Chartas et al. 2002, Pounds et al. 2003, but see Zoghbi et al. 2015) and might pose problems for theoretical acceleration models.

We adopt a redshift of $z = 2.473 \pm 0.001$ for J0230 based on visual inspection of the Lyα, C III], and Mg II emission lines and the onset of the Lyα forest. Our redshift is identical within the errors to the value of $z = 2.4721 \pm 0.0005$ given for this quasar in Pâris et al. (2014). We adopt a systematic uncertainty on the redshift of $\pm$0.0044, or 380 km s^{-1}. This uncertainty is the difference between the C III] emission-line redshift and the principal component analysis-based 'pipeline' redshift presented in Pâris et al. (2014); see that reference for details. If our adopted redshift is a slight underestimate due to blueshifting of the emission lines in our spectrum, it is conservative in the sense that it errs in the direction of minimizing the observed trough outflow velocities.

J0230 has an apparent magnitude of $g = 19.52$ and an absolute of $M_g = -27$. Because it is undetected in FIRST with an apparent magnitude of $i = 18.76$, it is not radio-loud ($R_i < 1$; see Figure 19 of Ivezić et al. 2002).

[2] We have determined the features claimed by Foltz et al. (1983) to be O VI at up to 70,000 km s^{-1} in the BAL quasar H 1414+089 are actually Si IVλ1062 and Si IV*$\lambda\lambda$1072,1073 absorption in a lower-velocity trough reaching only 28,000 km s^{-1}. That identification is secure because the object's Si IV+Si IV* trough shares the same distinctive 'double-dip' velocity structure as its C IV and N V troughs reaching 28,000 km s^{-1}; see Figure 2 of Foltz et al. (1983).

In section 2 of this paper, we outline our observations, data reduction methods, and spectral measurements. In section 3 we estimate the mass of the black hole. In section 4 we compare competing models of BAL variability in the context of our mulit-epoch data. Finally, we summarize our work in section 5.

Where needed, we adopt a flat cosmology described with $H_\circ = 70$ km s^{-1} Mpc^{-1}, Ω_M=0.3, and Ω_λ=0.7.

2 SPECTROSCOPIC DATA

2.1 Observations

J0230 was identified as having high-velocity absorption by visual comparison of its SDSS-I and SDSS-III spectra as part of a search for newly emerged BAL troughs whose results will be reported elsewhere. Follow-up observations were obtained using the Gemini Observatory (see Table 1 for a full list of observations). The Sloan Digital Sky Survey (SDSS; York et al. 2000) obtained two spectra of J0230 on MJD 52200 and 52942 using a 2.5 meter Ritchey-Chretien telescope located at the Apache Point Observatory in New Mexico. We retrieved the fully reduced spectra from the publicly available Data Release 7 (DR7) quasar catalog (Schneider et al. 2010). These spectra cover the wavelength range 3805−9221 Å and 3813−9215 Å, respectively, with a spectral resolution of $R \sim 2000$. The Baryon Oscillation Spectroscopic Survey (BOSS; Dawson et al. 2013), which is part of SDSS-III, obtained two more spectra of J0230 on MJD 55209 and 55455 using the same telescope as SDSS, but outfitted with a new spectrograph. We retrieved the fully reduced spectra from the publicly available Data Release 9 (DR9) quasar catalog (Pâris et al. 2012). These spectra cover the wavelength range 3574−10349 Å and 3594−10384 Å, respectively, with a similar spectral resolution to SDSS.

We observed J0230 on 15 August 2013 (MJD 56519) using the Gemini Multi-Object Spectrograph (GMOS) on the 8.1 meter Gemini North Cassegrain telescope located at the summit of Mauna Kea, Hawai'i. The B600 grating with 600 lines mm^{-1} was used set at a spectrum central wavelength of 460 nm (the Blaze wavelength is 461nm). Combined with a 1.0 arcsec wide longslit, the resultant wavelength coverage was 3143−6068 Å with a spectral resolution of $R \sim 1688$. The total exposure time was 1200 s. After noting variability of the broad absorption lines in these data, we observed J0230 on 23 December 2013 (MJD 56649) using GMOS on Gemini North. The instrument setup was identical as the previous observation, but with a longer integration time of 2500 s. The resultant wavelength overage was 3142−6077 Å with a spectral resolution of $R \sim 1688$. Finally, after noting further variability in J0230's broad absorption lines, we observed the object again on 28 January 2014 (MJD 56686) using GMOS on Gemini South, the twin telescope to Gemini North, located in Cerro Pachón, Chile. An identical instrument setup was used, with a total exposure of 2600 s, resulting in a wavelength coverage of 3145−6077 Å with a spectral resolution of $R \sim 1688$. All three Gemini observations were observed at the parallactic angle. The data were processed and extracted by standard techniques using the Gemini IRAF package. The relative fluxes for the three Gemini spectra were calibrated using spectrophotometric standard stars; the standard stars were not ob-

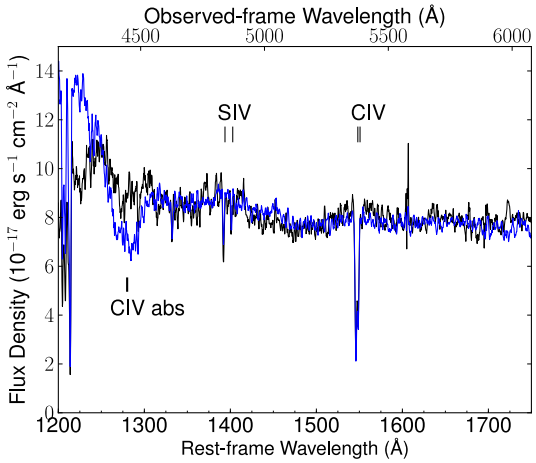

Figure 1. Spectra of J0230 at rest-frame wavelengths (bottom scale) and observed (top scale). The black spectrum is the mean SDSS spectra (see § 2.2.1). The blue spectrum was taken by BOSS on MJD 55455. The locations of the C IV and Si IV emission are labeled (though are weak). In comparing the spectra, a broad and deep trough was identified at roughly 1262−1302 Å. This trough was identified as highly blueshifted C IV absorption. This trough is referred to as trough A for the remainder of the paper. The Flux Density of the BOSS spectrum is artificially scaled up to match the continuum level of the SDSS spectrum for the purposes of visual comparison.

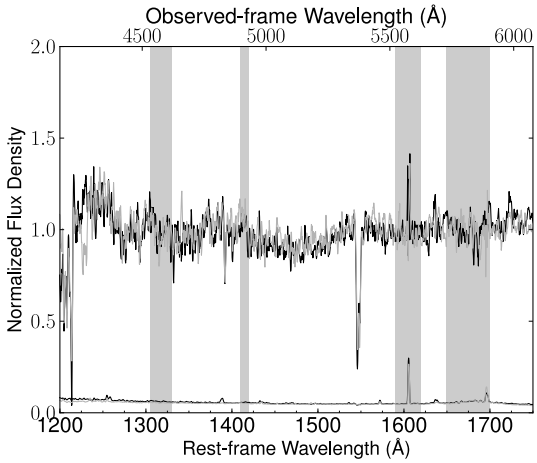

Figure 2. The normalized SDSS spectra. While there are some small differences between the two spectra (see description in § 2.2.1), since they do not interfere with the two troughs we study later we disregard them. As a result, we have combined the two SDSS spectra together for the analysis throughout the paper. The normalized error spectra are plotted at the bottom. The normalization windows are shown as gray regions.

served on the same night as J0230. See Table 1 for a list of observations and the nomenclature we have adopted throughout this paper.

In Figure 1 we plot the visual comparison of the mean SDSS spectrum (black; see § 2.2.1) and the BOSS2 spectrum (blue) that led to the identification of an emergent absorbing trough. The locations of the C IV and Si IV emission are given, though noted to be very weak (see § 2.3 for further discussion regarding Weak Line Quasars). The absorbing trough, which we refer to as trough A for the remainder of the paper, emerged at some point between the two spectral epochs and spans roughly 1260−1300 Å. We attribute this trough to C IV absorption by highly blueshifted gas outflowing along our line of sight to the quasar at approximately ∼56,000 km s^{-1}. We are confident trough A is not due to blueshifted Si IV absorption due to the lack of accompanying C IV expected at ∼1425 Å. Further, there is some evidence that trough A has accompanying N V absorption, which we discuss in § 2.3. We note there is a significant change in J0230's spectrum shortward of trough A, which is attributed to changes in the Lyα+N V complex in that region. Note that those changes do not affect our measurements on trough A throughout this work.

2.2 Normalization

In order to compare the changes we observed in the absorption features, we normalized each spectrum by a model of the underlying continuum. First, we smoothed each spectrum using a boxcar average over 5 pixels. Then we identified four regions that appeared unchanged across all 7 observations; hereafter, these are referred to as normalization windows. Lastly, we fitted a power-law continuum model to the windows using a least squares routine. The normalization windows we used were 1305−1330, 1410−1420, 1590−1620, and 1650−1700 Å. While there are other normalization windows that could have been used longward of ∼ 1700 Å for SDSS and BOSS, we refrained from using them because the Gemini spectra have significantly less spectral coverage. In order to compare the SDSS/BOSS spectra to the Gemini spectra we used normalization windows accessible from all data. We have visually inspected all our spectra and are confident these windows represent regions that are unchanged over all epochs of our observations. We note this is not a normalization in the traditional sense, as we did not fit the emission features.

Below we describe individual details for normalizing the SDSS, BOSS, and Gemini spectra.

2.2.1 SDSS Normalization

Two spectra of J0230 were taken on MJD 52200 and 52942, as part of the SDSS-I survey. In Figure 2 we present the normalized SDSS spectra; the gray regions indicated the normalization windows. The normalized error spectra are plotted along the bottom. Visual comparison show little difference between the two, with the small exception of apparent absorption at 1225−1235 Å present in the spectrum taken on MJD 52942, but not present in the previous epoch, taken on MJD 52200. This feature vanished by BOSS2 and never re-appeared, it is present only in our noisiest spectrum, and, most importantly, is not related to the two broad troughs that are the focus of this work. As a result, we do not consider it in this study. Other than this feature, there are little differences between the two SDSS spectra; we combined them into one (hereafter, 'the SDSS spectrum') in order to increase our signal to noise. We adopt an observation date for this combined spectrum of MJD 52942, that of the latter SDSS observation. Since no broad absorption is present in either of the SDSS spectra, we can confidently indicate this date to be the last time we observed no absorption present.

MJD_{Obs}	Rest Δt	Rest Day	Plate	Fiber	Origin	SN_{1675}	Name
52200.39	000.00	−866.02	705	407	SDSS-I	7.50	SDSS1
52942.34	213.63	−652.39	1509	365	SDSS-I	7.57	SDSS2
55208.10	652.39	000.00	3744	634	SDSS-III/BOSS	12.3	BOSS1
55454.46	71.93	71.93	4238	800	SDSS-III/BOSS	16.4	BOSS2
56519.53	306.67	378.06	...	...	Gemini-North	22.1	GEM1
56649.21	37.33	415.39	...	...	Gemini-North	23.2	GEM2
56685.07	10.32	425.71	...	...	Gemini-South	18.0	GEM3

Table 1. Spectroscopic observations of J0230. Rest Δt is the rest-frame time in days elapsed since the previous observation. Rest Day is cumulative rest days relative to the first BOSS observation. SN_{1675} is the median value of the normalized flux divided by the error in the flux over the spectral range 1650−1700 Å. The final column indicates how we will refer to each epoch for the duration of the paper.

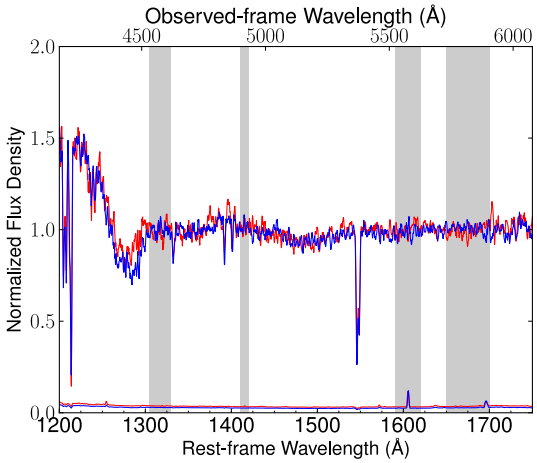

Figure 3. The normalized BOSS spectra. Since the high-velocity absorber at ∼1280 Å has changed between the two epochs, we cannot combine the BOSS spectra. The normalized error spectrum for both epochs is plotted at the bottom. The normalization windows are shown as gray regions.

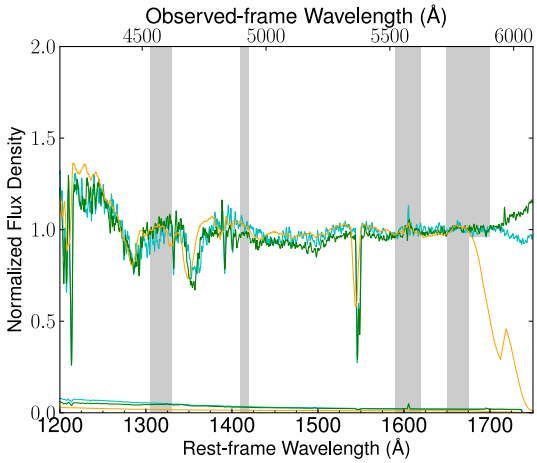

Figure 4. The normalized Gemini spectra. The normalization windows are indicated by the gray regions. The orange spectrum (GEM3) has slightly less coverage on the red end and thus we changed its third normalization window to 1640−1650 Å. The normalized error spectra for all three epochs are plotted at the bottom.

2.2.2 BOSS normalization

The BOSS survey observed J0230 two more times on MJD 55209 and 55455. We normalized these two spectra using the same normalization windows as were used for the SDSS spectra. In Figure 3 we plot the normalized BOSS spectra. In both BOSS epochs, trough A is present at ∼1280 Å. The absorption line varies between the two BOSS observations, thus we did not combine the two spectra as in the case of the SDSS spectra.

2.2.3 Gemini Normalization

Three Gemini spectra were taken on MJDs 56519, 56649, and 56685. In Figure 4, all three normalized Gemini spectra are plotted. In GEM1 we note the emergence of trough B, a separate medium-velocity absorber at 1350−1360 Å, which was not present in any of the SDSS or BOSS spectra. The Gemini spectrum taken on MJD 56685 (orange) exhibits less spectral coverage on the red side; the flux falls off quickly after ∼1675 Å. To account for this, the third normalization window used for this spectrum was 1640−1650 Å.

2.2.4 Final Spectra

The final six spectra (note the two SDSS spectra were combined) are plotted in Figure 5. For reference, the emission features for Si IV at ∼ 1400 Å and C IV at ∼ 1550 Å are marked; although both emission lines appear to be weak. In our collected data, we note two broad absorption features, labeled 'A' and 'B' in the figure. Trough A was first observed in the BOSS1 spectrum. At its widest (BOSS2) trough A spans 40 Å (1262−1302 Å). Trough B was first observed in GEM1. At its widest (GEM1) it spans 24 Å (1344−1368 Å). The legend of Figure 5 indicates the number of rest-frame days since the previous observation.

2.3 Summary of Spectral Features

In all spectra we obtained of J0230, the emission features are relatively weak compared to typical quasars; specifically, we measured the rest-frame equivalent widths (EWs) of the emission features: Lyα+N V= 8.0 ± 0.1 Å, Si IV < 1.8 Å, C IV < 2.5 Å, Al III+C III] = 6.1±0.2 Å, and Mg II = 9.8 ± 0.9 Å. When there is no apparent emission feature at the expected location of an ion, we measured the statistical noise in the spectrum in the ranges provided by the Vanden Berk et al. (2001) composite quasar spec-

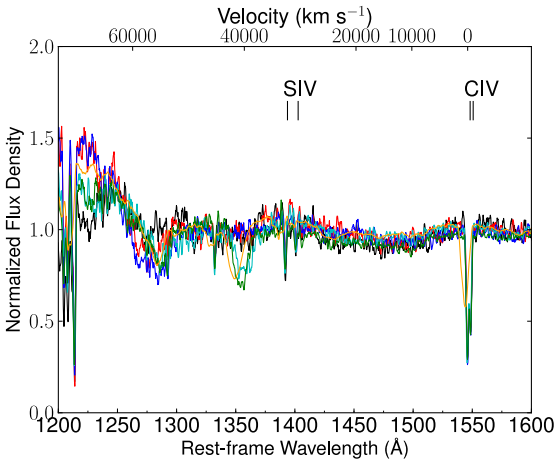

Figure 5. All 6 epochs of spectra plotted together. For reference, the emission features for Si IV at $\sim$ 1400 Å and C IV at $\sim$ 1550 Å are marked, as well as the two troughs 'A' and 'B' we observed to emerge during our monitoring campaign. In the legend the MJD of each observation is indicated as well as the number of rest-frame days since the previous observation. We also note the presence of a third mini-BAL feature labeled trough 'C' near the systemic redshift of the quasar. There was no significant change to trough C through all observations.

trum (see Table 2 therein). Specifically, they measured the Si IV EW over 1360−1446 Å, and the C IV EW over 1494−1620 Å. For those regions we measure the statistical noise in our spectra to be 0.60 Å and 0.84 Å, respectively. The upper limits quoted above are three times this statistical noise to indicate the largest possible EW these emission features could have that would still be statistically below the noise in our data. Also note that our measurement of Lyα+N V is contaminated by the Lyα forest; the actual EW is likely larger. In Luo et al. (2015), a Weak Line Quasar (WLQ) is defined as a quasar whose emission lines have rest-frame equivalent widths of <5 Å (they drew their sample of WLQs from Plotkin et al. 2010). While J0230 does not strictly meet the criterion laid in those works, its emission features are still far from a typical quasar's. The original WLQ, PG 1407+265, has emission features with comparable EWs to J0230 (McDowell et al. 1995, see Table 2 therein), as does the prototypical WLQ, PHL 1811, which which has the following EWs: Lyα+N V= 15 Å, C IV = 6.6 Å, Al III+C III] <4 Å, and Mg II = 12.9 Å (Leighly et al. 2007). Further, quasars with EWs < 10 Å investigated so far have sufficient similarities (e.g., common X-ray weakness) and can likely be unified as per Luo et al. (2015) in a common physical model. Therefore, we consider J0230 a WLQ.[3]

Also present in all spectra is a narrow C IV absorption feature at ∼1550 Å, very close to the systemic redshift of J0230 (also seen in Si IV, C II, N V, and Lyα), hereafter trough C. There were no dramatic changes in trough C in our observations.

[3] WLQs tend to have blueshifted broad emission lines in the UV, making systemic redshift determination more challenging than usual. Our adopted systematic redshift uncertainty of $\pm$380 km s^{-1} in J0230 is similar to the +300 km s^{-1}average difference between redshifts determined by narrow-line studies and those determined by SDSS for weak line quasars found by Plotkin et al. (2010).

The changes in the spectrum are best seen in Figure 6. In BOSS1 we note the appearance of trough A: a broad, high-velocity absorber covering the wavelength range 1260−1300 Å. Trough A grew to its strongest in BOSS2 by getting both deeper and wider; these changes were mostly in the the low-velocity half of the trough, whereas the high-velocity half of the trough changed less. In the first Gemini spectrum (GEM1), the high-velocity half of trough A weakened greatly while its low-velocity half weakened only somewhat, in comparison to BOSS2. Between GEM1 and GEM2, trough A strengthened slightly on its high-velocity side. We note in GEM1 the emergence of trough B, a second high-velocity absorber in the wavelength range 1344−1368 Å. We are confident this absorption is due to highly blueshifted gas along the line of sight to J0230. It cannot be due to blueshifted Si IV absorption because that would require accompanying C IV at ∼1500 Å. Further, there is some evidence to suggest there is accompanying Si IV and N V at similar outflow velocities (see below)y. Trough B's low-velocity end remained relatively unchanged (though slightly weaker) into GEM2, while its high-velocity side reached higher outflow velocities. Finally, between GEM2 and GEM3, trough A did not change appreciably, while trough B weakened on its low-velocity side and its high-velocity edge reached higher outflow velocities. Trough B also decreased in depth.

The presence of C IV absorption can be accompanied by absorption of one or more other ionic transitions, such as Si IV, Lyα, and N V. We searched for absorption of these ions that would correspond to the same outflow velocities as trough A or B. Figure 7 shows all 6 normalized spectra with a much heavier smoothing, and with a much wider wavelength coverage. We have marked the observed locations of the C IV absorption by trough A (dashed line) and by trough B (sold line), along with the expected locations of their accompanying Si IV, Lyα, and N V absorption. We have plotted the error spectra of the SDSS, BOSS, and GEM1 spectra along the bottom. For the purposes of clarity, the spectra were heavily smoothed in order to see features better in this more noisy part of the spectra. It is also of note the normalization was not repeated with new normalization windows in the region from 1000−1300 Å, thus the relative flux levels are not necessarily accurate. This is only meant to be a search for possible accompanying absorption.

For trough A, there appears to be no accompanying Si IV absorption in any of the spectral epochs we obtained. In searching for accompanying Lyα+N V, we note that the wavelength coverage does not extend far enough into the blue for SDSS, BOSS1, or BOSS2 but does for the three Gemini spectra. In these latter three epochs there may be N V, but no apparent Lyα is observed. For trough B, we note the possible presence of accompanying Si IV absorption in the three Gemini spectra, however, the absorption is coincident with the Lyα+N V emission systemic to J0230. Since it is very difficult to disentangle emission from coincident absorption, we cannot confirm this to be Si IV. The identification is also not certain because a flux deficit was also seen at that location in the SDSS spectrum, before trough B appeared. There is probable N V absorption for trough B.

Archival photometry of J0230 is available since it is located in Stripe 82, a region of sky imaged by SDSS, mul-

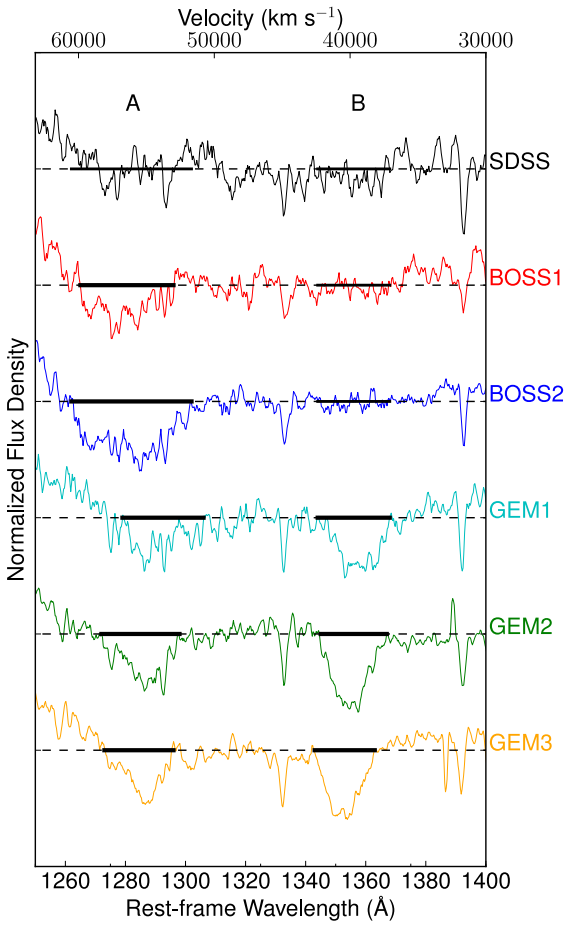

Figure 6. Each spectral epoch is plotted centred on the two absorbers, troughs A and B. We have separated the spectra artificially by 0.5 normalized flux units, with the earliest epoch (SDSS) at the top, and the most recent (GEM3) at the bottom. The dashed lines indicate the normalized continuum level for each spectrum. The black bars indicate where we define the absorption features to begin and end. Note for the SDSS spectrum, there is no apparent absorption in either troughs A or B. Also note for SDSS, BOSS1, and BOSS2 there is no apparent absorption for trough B. For these cases we have placed a slightly thinner black bar across the regions that represent the widest that trough became. For trough A, this occurs in BOSS2 and for trough B this occurs in GEM1.

tiple times over 7 years (MacLeod et al. 2010). We have obtained the photometry of J0230 from the SDSS archive, however, it is not concurrent with our spectroscopy. Thus it cannot help us interpret the spectroscopic variability we observe. J0230 was too faint for the Catalina Real-time Transient Survey (CRTS).

2.4 Measurements of Troughs A and B

We measure the properties of absorption troughs A, B, and C, such as the equivalent width (EW), the weighted centroid velocity v_{cent}, and the average trough depth, in all observations in order to compare changes from one epoch to the next.

In Figure 6, the 6 epochs of normalized spectra are plotted (separated artificially in the y direction). The bottom x-axis is the rest-frame wavelength, and the top x-axis is the outflow velocity relative to C IV ∼1550 Å. The dashed lines indicate the continuum for each spectrum. The dark horizontal lines indicate where we define absorption is present for troughs A and B (see below on how these were chosen).

To measure the EW from the normalized spectra we followed equations 1 and 2 in Kaspi et al. (2002), which are,

$$\mathrm{EW} = \sum_i \left(1 - \frac{F_i}{F_c}\right) B_i, \quad (1)$$

and the uncertainty on the EW is,

$$\sigma_{\mathrm{EW}} = \sqrt{\left[\frac{\Delta F_c}{F_c}\sum_i \left(\frac{B_i F_i}{F_c}\right)\right]^2 + \sum_i \left(\frac{B_i \Delta F_i}{F_c}\right)^2}. \quad (2)$$

F_i and ΔF_i are the flux and the error on the flux in the ith bin, F_c is the underlying continuum flux, ΔF_c is the uncertainty in the mean of the continuum flux in the normalization windows, and B_i is the bin width in units of Å. In our normalized spectra, $F_c = 1$ and ΔF_c is calculated using the windows 1305−1330 Å and 1410−1420 Å, which are the two windows closest to both absorption troughs. Thus σ_{EW} represents the statistical uncertainty inherent to the spectra. It does not quantify the systemic uncertainty, which is governed by the placement of the continuum by normalization.

The edges of troughs A and B in a given spectrum were identified by finding the locations where the flux drops below, and stays below, the normalized continuum level of $F_c = 1$. In Figure 6, these edges are represented by black horizontal bars; in Table 2, ΔW is calculated using these edges. We applied Equations 1 and 2 to calculate the EW within the edges found. We note that the placement of the normalized continuum, and thus the locations of the edges of the troughs, is highly sensitive to the normalization process. Further, for trough A, the absorption appears to be truncated by the Lyα+N V emission complex; as a result we consider our EW measurements to be conservative.

Note for both troughs, some epochs do not exhibit absorption; both troughs A and B are not present in the SDSS spectrum, and trough B does not exhibit absorption in the SDSS, BOSS1, and BOSS2 spectra. For these cases, we took the largest trough width determined for each trough and applied it to the unabsorbed spectra. For example, in the case of trough A, the widest the trough was observed to be was in the BOSS2 spectrum at $1262 - 1302 = 40$ Å. We applied this range of the absorption profile in the unabsorbed spectra of SDSS1 and measured the EW. The resulting value for the SDSS spectrum was -0.18 ± 0.48, indicating an EW consistent with zero. More examples of this can be found in Table 2 labeled with an ellipsis.

We measured the centroid velocity, v_{cent}, of the trough following the definition in Filiz Ak et al. (2013); it is the mean of the velocity in a trough where each pixel is weighted by its distance from the normalized continuum.

The mean depth of the trough was calculated in two ways. First, we measured d_{BAL} as in Filiz Ak et al. (2013), which is the mean distance from the normalized continuum level for each data point in the trough. Second, we

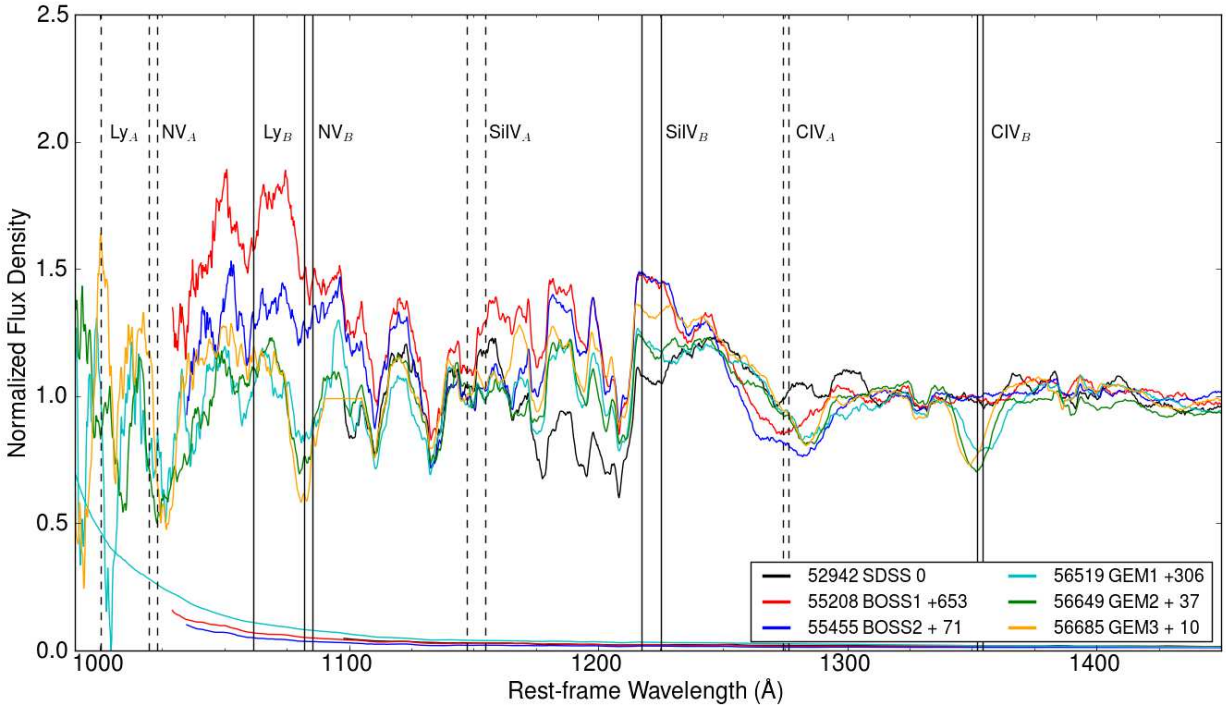

Figure 7. Plotted are the 6 normalized spectra with heavier smoothing (boxcar with window of 25 pixels) and with a much wider wavelength coverage. We have marked the location of the trough A C IV absorption with a vertical dashed line; the expected locations of Si IV, N V, and Lyαabsorption features that may accompany trough A's C IV are also marked with vertical dashed lines. The location of trough B's C IV absorption is marked with a vertical solid line, as are the expected locations of this features possible accompanying Si IV, N V, and Lyα. At the shortest wavelengths of the BOSS1 and BOSS2 spectra (at <1330 Å in the trough A rest-frame), the spurious broad 'emission' features are due to noise. It is of note these are the normalized spectra from § 2.2, which were created using continuum windows between 1300−1700 Å.

measured d_{max7}, which is calculated by sliding a 7 pixel-wide window across the trough and measuring the average depth over each window. We take the largest value of all these windows as d_{max7}. The uncertainty on the depth calculated as the uncertainty in the mean of the 7 pixels in the average. We note that since the our observations were taken with different telescope and instrument set ups, 7 pixels corresponds to slightly different resolutions; however, the differences are too small to impact the measurements. For reference, the 7 pixels covers approximately 2 Å, or ∼450 km s^{-1} in all spectra.

2.4.1 Coordinated Variability

Work on BAL quasar variability indicates troughs from the same object can vary in coordination with each other, which can lead to constraints on variability models (i.e., Filiz Ak et al. 2012, Wang et al. 2015; see discussion in § 4.1.1 below). We plot the EW of each trough vs. the rest-frame time elapsed since the SDSS epoch in Figure 8 and d_{max7} for each trough vs. the rest-frame time elapsed since the SDSS epoch in Figure 9 in order to investigate how the variability of one trough compares with the others. The EW of trough C remains relatively constant over all epochs. Both trough A and B begin with a very low EW, then emerge with a sharp and significant increase in later epochs (BOSS1 for A and GEM1 for B). There is an interesting pattern in the final three observations (the Gemini epochs), which occurs after both troughs have emerged and are established: the EW for both trough A and B increases for GEM2 and then returns to the same value it was in GEM1 for GEM3. This pattern could be interpreted as absorption from two physically distinct clouds varying in a coordinated fashion (for reference, the time frame from GEM1 to GEM3 is 47 days). However, the uncertainties on our EWs are of similar scale to the amount of variability we are referring to in the Gemini epochs. Thus, this pattern does not represent statistically significant coordination in variability.

2.4.2 BALnicity Index

For comparison to other BAL-quasar studies, we have measured the BALnicity Index (BI) of J0230. We calculate the Absorption Index (AI$_{450}$), defined in Hall et al. (2002), following:

$$\mathrm{AI}_{450} = \int_0^{v_{high}} \left(1 - \frac{f(v)}{0.9}\right) C' dv. \quad (3)$$

where $f(v)$ is the normalized flux density as a function of velocity, and C' is equal to 1.0 within a trough if the trough is wider wider widerthan 450 km s^{-1}, otherwise it is set to 0.0. The integration begins at v = 0 km s^{-1} relative to the systemic velocity of the quasar and runs through the highest velocity at which absorption is present.

We also measure the modified BALnicity index, BI*, following:

$$\mathrm{BI}^* = \int_{v_{low}}^{v_{high}} \left(1 - \frac{f(v)}{0.9}\right) C dv. \quad (4)$$

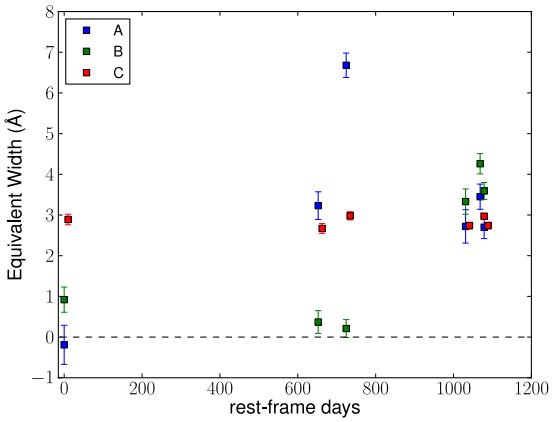

Figure 8. The measured equivalent widths (EW) for troughs A (blue), B (green), and C (red). The trough C points are artificially shifted to the right by 10 days in order to avoid confusion with trough A data points.

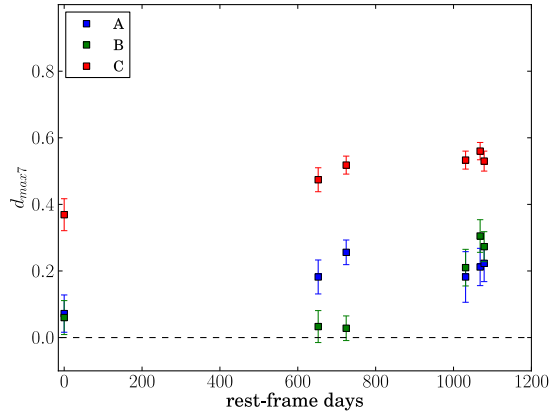

Figure 9. The maximum depth of trough A (blue), B (green), and C (red) as a function of rest-frame days. d_{max7} represents the lowest average 7 pixels in a row for each trough.

which is a modification of the original BI defined in Weymann et al. (1991) that imposes no constraint on the outflow velocity. BI* has no formal limit on the minimum and maximum absorbing velocities. The quantity C is equal to 1 only when the quantity in parentheses is greater than zero for more than 2000 km s^{-1}, otherwise it is set to 0.0.

In Table 3, we list the BALnicity indexes calculated using both methods. The total index value is measured over $v_{low} > 0$ and $v_{high} < 60,500$ km s^{-1}, however, we also provide the individual contributions of each trough in the spectra. Note that for AI$_{450}$, trough C contributes to the total index, but for BI* it does not.

3 BLACK HOLE MASS ESTIMATE

To estimate the mass of the SMBH in J0230, we used the velocity dispersion of the Mg II λ 2796, 2803 Å emission line. A full description of this technique can be found in Rafiee & Hall (2011). Equation 9 of that work is

$$M_{BH}/M_{\odot} = 30.5[\lambda L_{3000}/(10^{44}\ \mathrm{erg\ s^{-1}})]^{0.5}\sigma^2 \qquad (5)$$

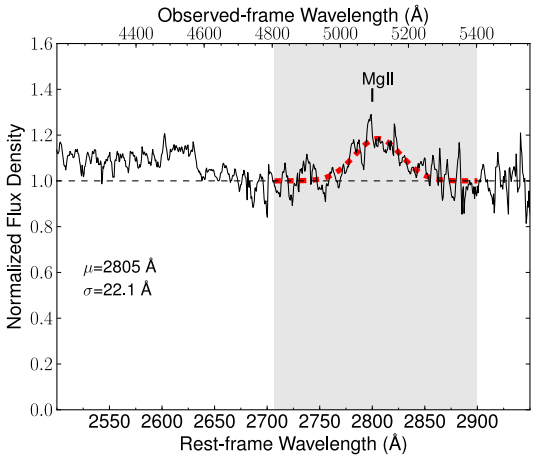

Figure 10. Combined BOSS spectra (black), continuum fit (dashed black), and Gaussian fit (dashed red) to the Mg II emission feature at $\sim$ 2800 Å. The fit was applied only to the data in grayed out region. The best-fit Gaussian parameters to the data are shown in the lower left.

where L_{3000} is the observed monochromatic luminosity at 3000 Å rest-frame, λ = 3000 Å, and σ is the intrinsic line dispersion of the Mg II emission line in km s^{-1}. There is intrinsic scatter of $\pm$0.15 dex ($\pm$35%) and systematic uncertainty of $\pm$0.10 dex ($\pm$24%) in this equation.

The two BOSS spectra of J0230 represent the best coverage we have of that wavelength regime. We combined the two BOSS spectra with a weighted mean, and then fit a line to the continuum using windows 2650−2700 Å, 2900−3000 Å. After fitting and removing the continuum, we fit a Gaussian to the remaining Mg II emission in the region 2700−2900 Å. In Figure 10 the fitted Gaussian is plotted over the normalized BOSS spectra. The best-fit parameters were μ = 2805 Å, and σ = 22.1 Å. The standard deviation in the Gaussian fit indicates the velocity dispersion of the Mg II emission feature, which is caused by the Doppler broadening of an AGN broad line region orbiting the SMBH. We convert σ = 22.1 Å = 2370 km s^{-1}.

To calculate the quasar luminosity we used

$$\lambda L_{3000} = 4\pi D_L^2 f_{3000} \times 3000(1+z), \qquad (6)$$

where D_L is the luminosity distance, f_{3000} is the observed flux density at rest-frame 3000 Å, and z is the redshift. We measured f_{3000} from the combined BOSS spectrum to be $f_{3000} = 3.35\times10^{-17}$ erg s^{-1} cm^{-2} (observed Å)$^{-1}$. For our adopted cosmology, the luminosity distance to $z = 2.473$ is $D_L = 2.01 \times 10^{10}$ pc, or 6.21×10^{28} cm. Therefore, we have $\lambda L_{3000} = 1.69 \times 10^{46}$ erg s^{-1}. Finally, we calculate the mass of the SMBH to be $M_{BH}/M_{\odot} = 2.2 \times 10^9$ with an intrinsic scatter of $\pm 0.8 \times 10^9$ ($\pm$35%).

For a SMBH of this mass the Eddington Luminosity is $L_{Edd} = 3.45 \times 10^{47}$ erg s^{-1}. Using a bolometric correction of $BC_{3000} = 5$ derived in Richards et al. (2006), this quasar has an estimated $L_{Bol} = 8.45 \times 10^{46}$ erg s^{-1}, and therefore this quasar has an estimated $f_{Edd} \equiv L_{Bol}/L_{Edd} = 0.25$. Such a black hole has $R_{Sch} = 6.6 \times 10^9$ km.

It is worth pointing out that Plotkin et al. (2010) present some evidence to suggest that some Mg II emission lines of WLQs could exhibit non-virialized behaviour (namely, the emission feature is blueshifted from the sys-

	Rest Δt	EW$\pm\sigma_{EW}$	Δw	Δv	d_{max7}	v_{cent}	d_{BAL}
Trough A	(days)	(Å)	(Å)	(km/s)		(km/s)	
SDSS	000.00	-0.19 ± 0.48	...	...	0.07 ± 0.06	...	...
BOSS1	652.39	3.23 ± 0.34	31	7002	0.18 ± 0.05	56496	0.10
BOSS2	71.93	6.68 ± 0.30	40	9028	0.26 ± 0.04	56004	0.17
GEM1	306.67	2.72 ± 0.41	27	6063	0.18 ± 0.08	53769	0.10
GEM2	37.33	3.45 ± 0.31	26	5860	0.21 ± 0.06	55020	0.13
GEM3	10.32	2.70 ± 0.28	23	5185	0.22 ± 0.06	55101	0.12
Trough B							
SDSS	000.00	0.92 ± 0.31	...	...	0.06 ± 0.05	...	...
BOSS1	652.39	0.37 ± 0.28	...	...	0.03 ± 0.05	...	...
BOSS2	71.93	0.21 ± 0.22	...	...	0.03 ± 0.04	...	...
GEM1	306.67	3.33 ± 0.31	24	5214	0.21 ± 0.05	39212	0.14
GEM2	37.33	4.26 ± 0.25	22	4780	0.31 ± 0.05	39726	0.11
GEM3	10.32	3.59 ± 0.21	20	4352	0.27 ± 0.04	40224	0.10
Trough C							
SDSS	000.00	2.89 ± 0.13	8	1549	0.49 ± 0.04	87	0.37 ± 0.05
BOSS1	652.39	2.67 ± 0.12	8	1550	0.47 ± 0.04	78	0.33 ± 0.05
BOSS2	71.93	2.98 ± 0.10	10	1935	0.52 ± 0.03	68	0.30 ± 0.05
GEM1	306.67	2.74 ± 0.08	7	1356	0.53 ± 0.03	163	0.39 ± 0.04
GEM2	37.33	2.97 ± 0.07	7	1356	0.56 ± 0.02	125	0.42 ± 0.04
GEM3	10.32	2.74 ± 0.08	7	1356	0.53 ± 0.03	212	0.39 ± 0.04

Table 2. Measurements made on trough A, B, and C. The '...' indicate where no absorption is visible in the spectrum. Values of EW for these cases used the widest possible ΔW the trough was observed to reach (BOSS2 for trough A, GEM1 for trough B).

	AI_A	AI_B	AI_C	total AI	BI^*_A	BI^*_B	BI^*_C	total BI*
SDSS	0.0	0.0	477 ± 3	477 ± 3	0.0	0.0	0.0	0.0
BOSS1	152 ± 5	0.0	437 ± 2	589 ± 5	0.0	0.0	0.0	0.0
BOSS2	746 ± 6	0.0	490 ± 2	1236 ± 6	561 ± 5	0.0	0.0	561 ± 5
GEM1	103 ± 6	323 ± 6	455 ± 2	880 ± 8	0.0	115 ± 4	0.0	115 ± 4
GEM2	293 ± 6	547 ± 6	491 ± 2	1331 ± 9	74 ± 4	242 ± 4	0.0	316 ± 5
GEM3	210 ± 6	433 ± 5	453 ± 2	1096 ± 7	35 ± 3	155 ± 3	0.0	190 ± 4

Table 3. The BALnicity was calculated using two different definitions: AI_{450} and BI* (see § 2.4.2). We calculated the total index over a velocity range of $v_{low} > 0$ and $v_{high} < 60,500$ km s^{-1}. We also calculated the individual contributions to the index by each trough in the spectra. In the case of AI_{450}, trough C contributed to the measurement; for completeness, we provide its index measurement. In BI*, trough C did not contribute to the total. Note the uncertainties quoted here are statistical only. Systematic uncertainty introduced by the placement of the continuum is not taken into account. A reasonable continuum uncertainty of $\pm5\%$ translates to a BALnicity Index uncertainty of $\pm5\%/d_{BAL}$.

temic redshift, though only by 360 km s^{-1} on average; see § 5.2 and 6.1 of that work). We see no such evidence of a non-virialized Mg II emission feature in J0230: a single Gaussian function fits the emission line well, its peak is actually redshifted by $\sim 510 \pm 380$ km s^{-1} from the position of Mg II expected from the composite spectrum of Vanden Berk et al. (2001).

Moreover, we have calculated black hole masses using the dispersion in the Mg II emission line for the objects from Plotkin et al. (2010). We find that the resulting masses are larger than the black hole masses they calculate using the dispersion in H β by only a factor of two. A deviation of that factor is not statistically significant given the uncertainties on our black hole mass estimate.

4 DISCUSSION

As mentioned in the introduction, broad absorption trough variability in quasars can be explained by transverse motion of the absorbing clouds across the line of sight to the accretion disk, or by changes in the ionization parameter of the absorbing cloud, or by a combination of these. Here we analyze two possibilities individually laying out constraints where possible. Note that in the end, the range of possible locations for the gas is large enough to preclude useful constraints on the kinetic luminosity of the outflow (Dunn et al. 2010), especially since the solid angle covered by this extremely high velocity outflow is unknown.

4.1 Pure Transverse Motion Variability Model

In the transverse-motion model it is assumed the absorption parameters of the cloud of gas are unchanged, and all

changes to the EW, the velocity profile, and the maximum depth of the trough can be explained by an absorbing cloud moving to cover more or less of the accretion disk. Any evolution of an absorption feature (i.e., an emergent trough) can be explained as long as the constraints from timescales yield plausible transverse velocities.

The transverse velocity of an absorbing cloud across the line of sight is derived by dividing the distance the cloud travels by the travel time it took to get there, the latter of which is time between successive observations. In order to measure the distance covered by an absorbing cloud between those observations we must both estimate the size of the continuum region it is traversing, and also model the relative sizes and shapes of the cloud and continuum region.

We approximate the continuum region to be represented by the α-disk model presented in Shakura & Sunyaev (1973), hereafter SS73, with the following model parameters. We set $\alpha = 0.1$, a free parameter in the model that governs the amount of accretion as a result of turbulence, typically $0 < \alpha < 1$. We assume a non-spinning black hole, which leads to an accretion efficiency of $\eta = 0.0572$. Given these parameters, the rate of mass accretion onto the black hole would be $\dot{m} \equiv f_{Edd}/\eta = 0.25$. Using an accretion disk defined by these parameters, we can estimate $D_{95}(1320)$, the continuum diameter within which 95% of the 1320 Å continuum is emitted. We use the 1320 Å continuum, which is the region in between troughs A and B, because it allows us to use a conintuum region that is the same size for both troughs; we note the size of the accretion disk would only change a small percentage if using the trough A or B centroid wavelengths. We find $D_{95}(1320) = 63\ R_{Sch}$, therefore, $D_{95}(1320) = 4.2 \times 10^{11}$ km. That gives a light-crossing time of 1.4×10^6 s = 16 days.

However, accretion-disk sizes inferred from gravitational-microlensing studies and photometric-reverberation studies (e.g., Morgan et al. 2010, Blackburne et al. 2011, Jiménez-Vicente et al. 2012, Edelson et al. 2015) are approximately a factor of four larger than the theoretical size predicted in the SS73 α-disk model (see a full discussion in Hall et al. 2013). Therefore, we increase our estimated continuum-source diameter by a factor of four, to $D_{95}(1320) = 252\ R_{Sch} = 1.7 \times 10^{12}$ km. The uncertainty in this number is likely a factor of two. A disk that size has a light-crossing time of 5×10^6 s = 64 days.

With the estimated size of the emitting region, and, given some simple models of clouds moving into or out of the line of sight of an emitting region, we can estimate a maximum and minimum transverse velocity of an absorption cloud that would be responsible for the emergence and variability of troughs A and B.

The most dramatic change we observed in the absorption depth of J0230 occurred in trough B when it emerged between the BOSS2 and GEM1 observations; the change in depth was $\Delta d_{max7} = 0.21 - 0.03 = 0.18$ over a period of 307 rest-frame days. As per the transverse-motion model, if we consider this change in depth to be entirely due to more of an optically thick absorbing cloud moving into the line of sight to the emitting region, it suggests that over 307 rest-frame days, the emitting region went from having 3% of its flux blocked to having 21% blocked, or a 21% covering fraction, C. Note in order for changes in absorption depth to equate to changes in covering fraction we are assuming the lines are optically thick. (If the lines are optically thin, the absorber must reach a larger covering fraction of the emission region in the same time span, requiring even higher transverse velocities.)

In Capellupo et al. (2013), two simple models were proposed for clouds crossing the emitting region (see Figure 14 therein). The first scenario is the 'crossing disks' model, where the absorbing cloud is projected on the sky as a circle (or a disk) and is crossing a circular emitting region (where the emitting region appears much larger than the absorbing cloud). In the second scenario the absorber is much larger than the background emitter it is traversing; this is the 'knife-edge' model. As mentioned above, the crossing speeds in these two scenarios are measured by dividing the distance traveled by the time it took to travel there. The change in covering fraction, ΔC, is the fraction of the emitting region the absorber crosses in the time-frame between observations. Therefore, in the 'crossing disks' scenario, the minimum distance traveled by the gas responsible for the emergence of trough B is $\sqrt{\Delta C} D_{95}(1320)$, and the crossing time is $\Delta t = 307$ days. Therefore, $\sqrt{0.18} \times 64$ light-days = 27 light-days in 307 days. Therefore the transverse speed is 26,400 km s^{-1}. However, if we assume the cloud has traversed to the exact opposite side of the emitting region, the distance traveled is the complete 64 light-days in 307 days. This results in a transverse velocity of 62,500 km s^{-1}. In the 'knife-edge' scenario, the distance traveled is $\Delta C\ D_{95}(1320) = 12$ light-days in 307 days. This equates to 11,700 km s^{-1}. Thus, given the above two scenarios, we can place the transverse velocity of a cloud responsible for the emergence of trough B in the range $11,700 < v(\mathrm{km\,s^{-1}}) < 62,500$. For trough A, the most dramatic change in absorption depth also occurred during its emergence, which was between SDSS and BOSS1; the change in depth was $\Delta d_{max7} = 0.18 - 0.07 = 0.11$ over a period of 652 rest-frame days. Applying the same relations as above we can place the transverse velocity of a cloud responsible for the emergence of trough A in the range $3,200 < v(\mathrm{km\,s^{-1}}) < 29,500$.

While these two models can be useful in interpreting observations in a campaign with two epochs, our unique dataset consists of six epochs. Analyzing the behaviour of the absorption features over all six epochs allows us to test the predictive power of the above two scenarios. For instance, trough B was consistent with zero absorption in the SDSS, BOSS1, and BOSS2 observations (see Table 2). The trough appeared between the observation of BOSS2 and GEM1, which was over a time period of 307 days, then for the next 2 observations (GEM2, and GEM3) the trough remained close to the same depth and EW (within the uncertainties). Assuming an absorber is moving at a constant velocity transverse to the line of sight, the above behaviour rules out the 'knife-edge' scenario, which would only cover more area as time goes on.

If we assume the emitting region has a uniform flux across its area (as Capellupo et al. 2013 does), then the 'crossing disk' scenario can explain trough B's behaviour. However, research into the theoretical understanding of accretion disks - through the work of SS73 and Dexter & Agol (2011) (among others) - indicates the emitting region is unlikely to be homogeneous. If we assume the emitting region is more like a SS73 disk, where the majority of the

flux is concentrated toward the centre of the emitting region, we can also rule out the 'crossing disks' scenario.[4] A crossing disk of fixed size traversing a SS73 accretion disk at a constant velocity would produce an increasing amount of observed covering fraction as it moved across the first half of the disk, but then a decreasing amount of covering as it traversed the second half of the disk. If trough B appeared in GEM1 as a result of transverse motion, we would have expected to see the depth of the absorber decrease appreciably in the subsequent observations of GEM2 and GEM3. Since this is not the case, the 'crossing disks' scenario is unlikely to be the correct interpretation of the variability of trough B.

Over 6 epochs, the nature of trough A's variability also rules out the 'knife-edge,' but agrees with the augmented 'crossing disks'+SS73 scenario. Specifically, there was no measured absorption in SDSS after which there was an increase in absorption in BOSS1 which continued to increase in both depth and EW into BOSS2. Then by GEM1 through GEM3, both the depth and EW returned back to values similar to those measured in BOSS1. This is consistent with a cloud smaller in angular size than the emitting source traversing into the line of sight for BOSS1, crossing the central portion of the disk leading to a the measurements of BOSS2, continuing on to the second half of the disk for GEM1 and GEM2, but has not reached the other side yet as there is still measured absorption in GEM3. If we apply the relations from the 'crossing disks' scenario above, the velocity range this absorber would have is $10,000 < v\ (\mathrm{km\,s^{-1}}) < 18,000$. At 18,000 $\mathrm{km\,s^{-1}}$ we expect trough A to disappear completely approximately 350 days after the GEM3 observation. At 10,000 $\mathrm{km\,s^{-1}}$ we expect it to disappear approximately 1,500 days after the GEM3 observation.

There is one plausible scenario of transverse motion that can match the observed depth changes in trough B in the context of a SS73 disk: a 'flow-tube' (similar to that proposed by Arav et al. 1999; see their Figure 10). In Figure 11, we have plotted a log-luminosity map of an accretion-disk emitting at 1320 Å powered by a SMBH equal to that of J0230 (see § 3). The emitted light is much more concentrated towards the centre (though note there is a region occupied by the black hole where no emission is observed). We have plotted over top of the map an example of our proposed flow-tube scenario. The tube is traversing the continuum region at some impact parameter, i, away from the centre, and has some width, w. The tube extends infinitely to the left in this figure. We note that our flow-tube geometry and dynamics differ from that proposed in Arav et al. (1999). Specifically, we have chosen a flow-tube that is homogeneous from centre to edge and is in the midst of establishing itself along our sight-line before settling into a long-term configuration as discussed in Arav et al. (1999).

If a flow-tube similar to the one shown in Figure 11 were to move across the emitting region of J0230, it would serve to create a sharp increase in absorption as it crossed close to the centre of the disk, but due to there being very little flux at the edges of a SS73 disk, not much more coverage would occur as it traversed the second half of the continuum region. This geometry would match the behaviour we see in the variability of trough B.

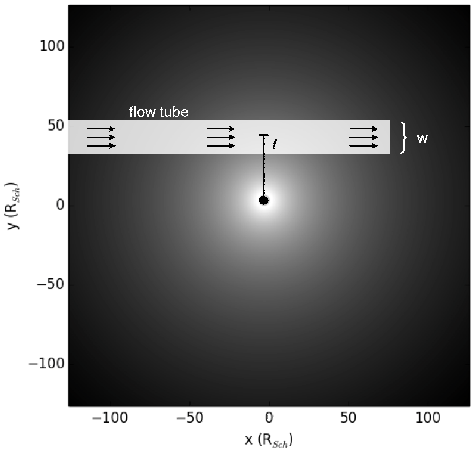

Figure 11. An example of a flow-tube traversing a simulated emitting region of an accretion-disk. The logarithm of the luminosity of the disk is represented by the gray scale. Over-plotted is an example of a flow-tube traversing the disk, which would serve to cover some of the light, creating absorption. In this representation, the tube extends infinitely to the left but terminates at the right edge drawn. The width of the tube is w and the impact parameter relative to the centre of the accretion disk is i. Note there is a region at the very centre occupied by the black hole where no luminosity is observed.

We have investigated whether a flow-tube of this nature could successfully reproduce the variability in trough B, and at what velocities it could do this, by simulating flow-tubes of various widths and impact parameters traversing a SS73 disk, measuring how much flux is covered as a function of distance across the disk the simulated flow-tubes produce, and then attempting to match the observed covering fractions for trough B to the simulated covering fraction vs. distance generated by the flow-tubes. Referring to Figure 11, traversed distance is measured along the x-axis of the disk, and the direction of motion of each simulated flow-tube is from the negative x direction towards the positive x direction.

Matching the observations to our simulations was done via the following prescription: A given simulated flow-tube has covering fraction as a function of x, $C(x)$. We search for a distance across the accretion disk, x_0, that matches the covering fraction for BOSS2, namely $0 < C(x_0) < C(\mathrm{BOSS2})+1\sigma$, which is the last time trough B was measured to have a depth consistent with zero. When found, we go searching for the next closest x_1 that satisfies $C(GEM1) - 1\sigma < C(x1) < C(GEM1) + 1\sigma$. We calculated the velocity, v, required to cover the distance from x_0 to x_1, given the known time between successive observation (307 days from BOSS2 to GEM1). We then searched for the next x_2 that satisfies $C(GEM2) - 1\sigma < C(x_2) < C(GEM2) + 1\sigma$. When a match is found, we use the simulated distance from x_1 (GEM1) to x_2 (GEM2), and the velocity the flow-tube is moving at, v calculated above, to determine the length of time it would take for the flow-tube to cover the distance $x_1 - x_2$. If the time is equal to the time between GEM1 and GEM2 observations (37 days) then we continue the search to see if GEM3 also matches. We look for x_3 that satisfies $C(GEM3) - 1\sigma < C(x_3) < C(GEM3) + 1\sigma$. Sim-

[4] see Fig. 11 for an example of the luminosity gradient of a SS73 accretion-disk; this figure will be discussed in more detail later

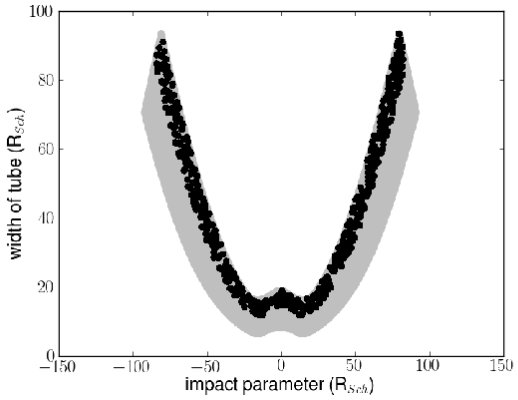

Figure 12. Width of flow-tube vs. the distance from centre of accretion disk the flow-tube traverses (impact parameter). It is plotted in units of $R_{Sch} = 6.6 \times 10^9$ km. The gray region represents all possible combinations of flow-tubes that resulted in a final covering fraction between 15% and 30%. The black points are the combinations of parameters that not only matched all covering fractions in our observations, but did so within the observation time constraints. The x-axis is plotted is distance from centre of tube to centre of accretion disk, where positive and negative values represent opposite sides of centre.

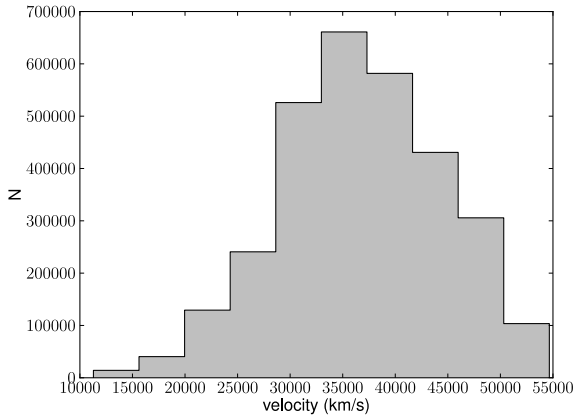

Figure 13. The range of possible velocities of a flow-tube traversing the emitting region of J0230. These were determined by simulating flow tubes of various widths and impact parameters across a SS73 disk scaled to match J0230's mass and monochromatic luminosity at 1320 Å. In order to be a plausible velocity, the tube must recreate the covering fraction at each spectral epoch, given one velocity, as well as match the time between observations.

ilar to above, we use the distance from x_2 (GEM2) to x_3 (GEM3), and the v above to determine the length of time it would take for the flow-tube to cover that distance. If that time is equal to the time between GEM2 and GEM3 observations (10 days) then we have found a combination of width and impact parameter for a simulated flow-tube that matches the variability in covering fraction as well as the time between successive observations. In Figure 12, we have plotted the parameter space of width vs. impact parameter that we investigated with the simulated flow-tubes. The gray region displays the combinations of parameters that resulted in a flow-tube's final covering fraction (after it had completely traversed the disk) between 15% and 30%, which is a healthy margin for the GEM3 covering fraction. The black points represent the combinations that fit the variability of BOSS2 through to GEM3. In Figure 13 we plot a histogram of all possible velocities we determine from the above analysis. The mean velocity of the distribution is $36,800$ km s^{-1} with a range spanning $8,000 < v\ (\mathrm{km\,s^{-1}}) < 56,000$.

Trough A could still be explained as a flow tube, but a simple flow tube model is not consistent with its d_{max7} and EW variations. The best fit despite those variations would yield a slower transverse velocity because the time over which the biggest change occurred (SDSS-BOSS1) is larger than for trough B. Note that a slower transverse velocity is consistent with trough A's higher line-of-sight velocity, as gas which is closer to terminal velocity is likely farther from the quasar with lower transverse velocity due to angular momentum conservation.

In summary, we have found that pure transverse motion can plausibly explain the variability of both trough A and B over all 6 epochs of observation in our dataset. Trough A is best explained by a 'crossing disks' traversing a SS73 disk at velocities between $10,000 < v\ (\mathrm{km\,s^{-1}}) < 18,000$. This model and velocity range allow us to predict trough A will disappear between $350 < t$ (days) $< 1,500$ after our last observation (GEM3). Trough B is best explained by a flow-tube that has recently moved into the line of sight, travelling in the velocity range $8,000 < v\ (\mathrm{km\,s^{-1}}) < 56,000$. In this scenario, we have no constraint on how far a flow-tube extends, and thus cannot predict when trough B will disappear.

4.1.1 Constraining Distances

If we assume the absorbers responsible for both trough A and B have reached maximum velocity, have transverse velocities v_{trans} and we are observing them at some current distance r_C from the BH, but was launched from a circular orbit at a distance r_L, which has an orbital velocity $(GM_{BH}/r_L)^{0.5}$, then we can constrain both r_C and r_L using our observed velocities. From conservation of angular momentum for a gas parcel of mass m, we have

$$m \times r_L \sqrt{\frac{GM_{BH}}{r_L}} = m \times r_C v_{trans}. \quad (7)$$

Thus the BAL gas transverse velocity is $v_{trans} = \sqrt{GMr_L/r_C^2}$ (ignoring any transverse component of its velocity away from the black hole across our line of sight to the continuum source). The final radial velocity is $v_\infty = F\sqrt{GM/r_L}$ where the scaling factor F is $1.5 < F < 3.5$ if the wind is accelerated by radiation pressure on ions in dust-free gas (see Murray et al. 1995; Laor & Brandt 2002; Baskin et al. 2014). To solve for r_L and r_C, we take

$F = 2.5 \pm 1.0$ and assume that the observed radial velocity $v_{rad,obs}$ equals the terminal velocity v_∞. If the latter assumption is incorrect, the true r_L will be smaller, so we call the value we obtain with that assumption $r_{L,max}$. Given the minimum velocity determined for trough A above, $v > 10,000$ km s^{-1},we find $r_{L,max} = 78^{+74}_{-50}$ R_{Sch} = $0.02^{+0.02}_{-0.01}$ pc and $r_C \leqslant 186 \pm 75$ $R_{Sch} = 0.04 \pm 0.02$ pc, where the uncertainties on the values of the radii correspond to the values assumed for F. The minimum velocity determined for trough B above was 8,000 km s^{-1}, which yields $r_{L,max} = 175^{+165}_{-115}$ $R_{Sch} = 0.04^{+0.04}_{-0.02}$ pc and $r_C \leqslant 350 \pm 75$ $R_{Sch} = \pm 3$ pc.

4.1.2 Acceleration

The above estimate of $r_{L,max}$ assumes that the gas producing trough B has reached maximum velocity, which may or may not be correct. Here we explore some implications if that assumption is incorrect. At the small radii inferred above, the gas may still be accelerating. We can make an order of magnitude estimate of the expected acceleration using some simple assumptions. We stress that these assumptions are not unique, only illustrative.

The radial velocity of a radiatively-accelerated wind is approximately $v(r) = v_\infty(1 - r_L/r)^{1.15}$ (Murray & Chiang 1997). The acceleration of the wind is

$$a(r) = \frac{dv}{dt} = v\frac{dv}{dr} = 1.15\frac{v_\infty^2 r_L}{r^2}\left(1 - \frac{r_L}{r}\right)^{1.30}. \quad (8)$$

If we assume a terminal velocity of v_∞ = 60,000 km s^{-1} for trough B, because the observed velocity of trough A shows that C IV absorption can be seen to that high a velocity, then $r_L = 78^{+75}_{-50}$ R_{Sch}. If we set trough B's observed velocity $v_{rad,obs} = 40,000$ km s^{-1} = $v(r_C)$, we find $r_C = 3.4 r_L = 265^{+255}_{-170}$ R_{Sch}. (Incidentally, that yields a transverse velocity for trough B of $v_{trans} = 7,200^{+3000}_{-2100}$ km s^{-1}, consistent with the lower limit on the transverse motion velocity we determined for a flow-tube in § 4.1). The expected acceleration at $r_C = 265$ R_{Sch} for a wind launched at $r_L = 78$ R_{Sch} is 35^{+17}_{-11} km s^{-1} day^{-1} (the maximum acceleration in that model is 86 km s^{-1} day^{-1}).

This value is much larger than previous measurements of accelerating BAL winds. For example, Hall et al. (2007) measured an acceleration in a C IV trough found in SDSS J024221.87+004912.6 at approximately 0.1 km s^{-1} day^{-1}. The acceleration in J0230, if confirmed, would be the largest ever detected in a BAL outflow.

Using the Gemini South telescope, we have obtained a new spectral epoch of J0230 roughly 100 rest-frame days after the GEM3 epoch of this work. If the above transverse motion variability model is correct, then we predict trough B's centroid velocity will have increased in velocity by $3,500^{+5200}_{-2400}$ km s^{-1} in that data. The results of the new observations will be presented in a future paper (Rogerson et al., in preparation).

This analysis was not done for trough A because we have no reliable terminal velocity to suggest the cloud might accelerate to.

4.2 Pure Ionization Parameter Variability Model

In this model, we assume the absorbing clouds are not moving across the emitting region of the quasar, and thus any variability observed in troughs A and B is due to changes in the ionization parameter of the absorbing clouds. In Filiz Ak et al. (2012, 2013), the authors observed coordinated variability of distinct C IV BAL troughs in the same quasar, even if the troughs are separated by as much as 10,000−20,000 km s^{-1}. Other studies, such as Grier et al. (2015), observed BAL troughs to vary across the entire trough, rather than distinct sections. We do not observe either of these behaviours in J0230: we find no significant evidence for coordinated variations between troughs A and B (they are separated by ∼15,000 km s^{-1}), and we observe distinct regions of the absorption profiles to vary, while others do not (specifically in trough B, see § 2.4.1). Nevertheless, if we assume the changes observed in the troughs are due to an ionization state change, we can place constraints on the physical properties of the absorbing gas. Note that in this model only fully saturated troughs will not vary.

The two absorbers responsible for troughs A and B cannot have the same distances and densities (including density as a function of velocity) to explain the two trough's different responses to the same underlying ionizing flux. The exception would be if the absorber closer to the quasar significantly reduces the ionizing flux reaching the absorber farther away. Whether the effect is significant or not depends on the optical depth to ionizing radiation of the absorber closer to the quasar.

Below, we assume that faster-responding gas has higher density. If the changes in trough A are due purely to ionization parameter variability, then the high-velocity part of this trough has higher density (it responded more quickly, and then vanished). If the changes in trough B are due purely to ionization parameter variability, then the low-velocity part of trough B has higher density (it responds faster to ionizing flux changes), and the density drops off with increasing velocity.

One possible pure ionization variability scenario is the following. Prior to SDSS, the ionizing flux F_{ion} was high, leading to weak absorption. Between SDSS and BOSS1, F_{ion} decreased, leading to an increase in C IV absorption (dense trough A appears). After BOSS2, F_{ion} recovered somewhat, leading to weaker trough A absorption. Between BOSS2 and GEM1, lower-density trough B appears in response to the earlier decrease in F_{ion}. The above scenario suggests that, barring any major future ionizing flux variability, both trough A and trough B will decrease in strength with time. Any other trough that appears will show slower evolution in its EW than trough B does, due to the new trough's required lower density.

4.2.1 Ionization constraints on electron density and distance

Constraints can be placed on the distance from the continuum source to the absorbing gas, as well as the density of that gas using the timescale of the variability in the absorption. This approach has been used in multiple works (see Hamann et al. 1995, Hamann et al. (1997), Narayanan et al. (2004), Arav et al. 2012, and references

therein). Below, we reproduce the approach taken in Grier et al. (2015).

Consider gas initially in photoionization equilibrium in the case where the ionization rate out of ionization stage i changes from its equilibrium value I_i to $(1+f)I_i$, and the rate out of stage $i-1$ changes from I_{i-1} to $(1+f)I_{i-1}$,[5] where f is the fractional change in I_i. Immediately after this change:

$$\frac{dn_i}{dt} = -fn_iI_i + fn_{i-1}I_{i-1} + [-n_i(I_i + R_{i-1}) + n_{i-1}I_{i-1} + n_{i+1}R_i = 0] \quad (9)$$

where the quantity in brackets is the equilibrium value of $\frac{dn_i}{dt}$ and is therefore zero. In equilibrium, $n_{i+1}/n_i = I_i/R_i$ where R_i is the recombination rate to stage i, because appearance/increase of stage i by recombination from stage $i+1$ must be balanced by appearance/increase of stage $i+1$ by ionization from stage i. Thus we can substitute $n_{i-1}I_{i-1} = n_iR_{i-1} = n_i\alpha_{i-1}n_e$ (using $R_{i-1} = \alpha_{i-1}n_e$, where α_{i-1} is the recombination coefficient to stage $i-1$) and rewrite $\frac{dn_i}{dt}$ as

$$\frac{dn_i}{dt} = -fn_iI_i + fn_i\alpha_{i-1}n_e \quad (10)$$

which can be written as

$$\frac{dn_i}{n_i} \equiv \frac{dt}{t_i^*} \text{ with } t_i^* = [-f\,(I_i - n_e\alpha_{i-1})]^{-1} \quad (11)$$

which is an equation for variations on a characteristic timescale t_i^*: $n_i(t) = n_i(0)\exp(t/t_i^*)$.

To summarize, for gas which is initially in photoionization equilibrium, the characteristic timescale for density changes in ionization stage i of some element in response to an ionizing flux change can be written as t_i^* above (a modified version of Eq. 10 of Arav et al. 2012), where $-1 < f < +\infty$ is the fractional change in I_i, the ionization rate per ion of stage i [$I_i(t>0) = (1+f)I_i(t=0)$], α_{i-1} is the recombination coefficient to ionization stage $i-1$ of the ion, and a negative timescale represents a decrease in n_i with time. Note that this equation only considers photoionization processes; collisional processes are neglected. Gas which shows varying ionic column densities is not in a steady state by definition, but such gas can still be in equilibrium with a varying ionizing flux if its t_i^* is considerably shorter than the flux variability timescale (§ 6 of Pietrini & Krolik 1995). For optically thin gas at distance r from a quasar with luminosity L_ν at frequency ν, the ionization rate per ion of stage i is given by

$$I_i = \int_{\nu_i}^{\infty} \frac{(L_\nu/h\nu)\sigma_\nu}{4\pi r^2} d\nu \quad (12)$$

where σ_ν is the ionization cross-section for photons of energy $h\nu$.

If the absorbing gas is far enough from the quasar that $I_i \ll n_e\alpha_{i-1}$, then the relevant timescale is $t_{rec} = 1/fn_e\alpha_{i-1}$ (which is just the recombination time of the ion in the $f=-1$ case where the ionizing flux drops to zero), and the observed absorption variability timescale constrains the density of the absorber. However, if the absorbing gas is close enough to the quasar that $I_i \gg n_e\alpha_{i-1}$, then the relevant timescale is $t_i = -1/fI_i$ and the absorption variations of the ion reflect the ionizing flux variations of the quasar, with no density constraint derivable just from absorption variations.[6] An observed timescale for variations in optically thin absorption therefore constrains the absorbing gas to either have a density $n_e > n_{min}$ and $r > r_{equal}$, where r_{equal} is the distance at which $I_i = n_{min}\alpha_{i-1}$, or to be located at $r < r_{equal}$ with almost no constraint on the density.

As noted in Arav et al. 2012, there are limitations to using timescale arguments to infer physical characteristics of an absorber. In that work, the authors indicate "a more physically motivated approach is to use lightcurve simulations that are anchored in our knowledge of the power spectrum behaviour of observed AGN lightcurves;" however, such detailed work is not justified by the relatively scarce data available for J0230.

To determine the constraints on the emergence of troughs A and B, we assume a temperature of $\log T = 4.3$ (Krolik 1999) so that the recombination coefficient is $\alpha_{C\,III} = 2.45 \times 10^{-11}$ cm^3 s^{-1} (from the CHIANTI online database; see Dere et al. 1997, Landi et al. 2013). For the simple case of the ionizing flux dropping to zero, $f=-1$ and the timescale t_i^* can be approximated as the recombination time, $t_{rec} \sim 1/n_e\alpha_{C\,III}$.

Using the time between observations of SDSS and BOSS1 for trough A of 652 days as an upper limit to the recombination time, we calculate a lower limit on the density of the gas to be $n_{e,A} \geqslant 724$ cm^{-3}. Using the lower limit density of $n_{e,A} \geqslant 724$ cm^{-3}, we calculate the minimum distance from the quasar at which that lower limit is valid. From its observed flux density at rest-frame 3000 Å, our quasar has $L_{bol} = 8.45 \times 10^{46}$ erg s^{-1}. We adopt the spectral energy distribution of Dunn et al. (2010) to calculate L_ν. Therefore, if the emergence of trough A is due to ionization variability, the absorber either has a density of $n_{e,A} \geqslant 724$ cm^{-3} and is at $r_{equal,A} \geqslant 2.00$ kpc, or is at $r < 2.00$ kpc with no constraint on the density.

Trough B emerged between BOSS2 and GEM1; a period of 307 days. Using this as an upper limit to the recombination time, we perform the same calculation and determine if the appearance of trough B is due to ionization variability, the absorber either has a density $n_{e,B} \geqslant 1540$ cm^{-3} and is at $r_{equal,B} \geqslant 1.37$ kpc, or is $r < 1.37$ kpc with no constraint on the density.

Our values for n_e are one or two orders of magnitude lower than those found in Grier et al. (2015) and Capellupo et al. (2013) (which found values $\sim 10^5$ cm^{-3} and our values of r_{equal} are 10 times larger those works (which found values ∼100 pc). Further, our values of r_{equal} are much higher than the launching radius of BAL winds expected from theoretical work, which predict $\sim 10^{-3}$ pc (e.g., Murray et al. 1995). Nonetheless, other works have reported outflow radii on similar scales to that we infer for J0230 in a pure ionization variability

[5] Where we have assumed the fractional change for I_i and I_{i-1} is the same.

[6] No constraint on n_e is derivable even though we can write the timescale as

$$t_i^* = \left[-f\alpha_i n_e \left(\frac{n_{i+1}}{n_i} - \frac{\alpha_{i-1}}{\alpha_i}\right)\right]^{-1} \quad (13)$$

(see equation (2) in Hamann et al. 1997, equation (3) in Arav et al. 2015) because in our case $n_{i+1}/n_i = n_{\rm C\,V}/n_{\rm C\,IV}$, and that ratio increases more rapidly than n_e decreases as the ionization parameter increases (Kallman & McCray 1982).

model (see Table 10 of Dunn et al. 2010, and references therein), and the radius at which a BAL wind is observed is not necessarily the radius at which the wind is launched (e.g., Faucher-Giguère et al. 2012).

Finally, we can place an upper limit constraint on n_e by searching for absorption features from other ions of carbon, specifically C II λ1335 Å. Given the minimum density and r_{equal} distances determined above, troughs A and B are created by absorbers with an ionization parameter of $U_H \simeq 0.06$.[7] If we lowered the ionization parameter by a factor of ∼50, either by gas at larger radii or at higher density, the resulting ionization state would yield C II absorption roughly half as deep as the observed C IV (see Figure 3 of Hamann et al. 1995).

A reduction by a factor of ∼50 in ionization parameter gives us upper limits to both the minimum density and the r_{equal}; Therefore, the absorber that caused the emergence of trough A has 724 cm^{-3} $\leqslant n_{e,A} \leqslant$ 3.62 $\times$ $10^4(r_{equal,A}/r)^2$ cm^{-3} and is between $r_{equal,A} \leqslant r \leqslant 7r_{equal,A}$. Similarly, the absorber that caused the emergence of trough B is constrained by 1540 cm^{-3} $\leqslant n_{e,B} \leqslant$ $7.70\times10^4(r_{equal,B}/r)^2$ cm^{-3} and $r_{equal,B} \leqslant r \leqslant 7r_{equal,B}$. These upper limits only work in the scenario where we approximate the recombination time as $t_{rec} \sim 1/n_e\alpha_{C\,III}$.

In Figure 14, we have plotted the possible values of the density of the absorbing gas n_e and the distance the absorber is from the source r, given constraints imposed by the timescale arguments above for trough B. The vertical and horizontal dashed lines are the locations of the $r_{equal,B}$ and the minimum electron density $n_{e,B}$, respectively. Any combination of parameters above the red line would have too high a density or too far a distance to be ionized to C IV (and lead to the upper limit arguments above). There is also a region of too low density or too far away that requires too long a timescale for the proper response. The allowed regions 1 (between the red and blue curves) and 2 (to the left of the green curve) represent the combinations of parameters possible. There is also a region of too high ionization at low densities and small radii which is not visible at the scale shown. Note that in the discussion at the end of § 4.2 we assumed that faster-responding gas has higher density, although from Figure 14 that is only certain if the gas is at $r > r_{equal}$. A corresponding plot for trough A would look similar.

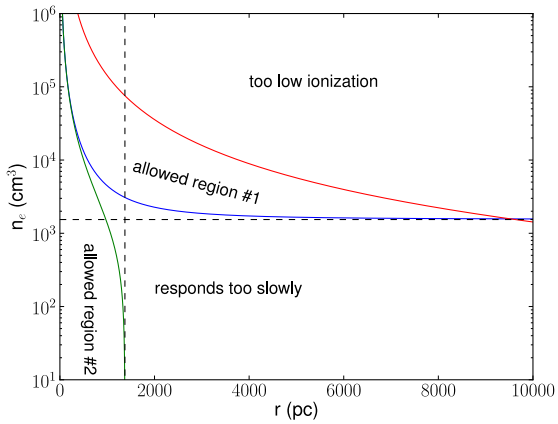

Figure 14. The possible combinations of density and distance for the gas that created trough B. The horizontal dashed line represents the density if the ionizing flux dropped to zero and we use the time between observations as the recombination time. The vertical dashed line represents minimum distance from the quasar at which the lower limit to the density is valid.

5 SUMMARY

We have presented the discovery and analysis of two extremely high-velocity and highly-variable C IV BAL troughs in the quasar SDSS J023011.28+005913.6. We retrieved 4 spectra of J0230 from the SDSS+BOSS archives, and obtained 3 of our own spectra using the Gemini Observatory. The longest time between observations was ∼ 650 rest-frame days, and the shortest was ∼ 10 rest-frame days.

(i) We discovered a C IV BAL trough outflowing from J0230 at ∼60,000 km s^{-1} (trough A), the largest velocity of a BAL wind observed to-date. During follow up observations, we discovered a second C IV BAL trough outflowing at ∼40,000 km s^{-1} (trough B). See Figure 5.

(ii) In troughs A and B we observed variability of both the depth and shape of the troughs on scales as short as 10 days in the rest-frame. See Table 2.

(iii) A dataset of six spectral epochs straddling the emergence of both troughs allowed us to rule out some simple models of bulk motion as the origin of the variability. It also allowed us to propose and test more complex and realistic models of bulk motion, such as flow-tube geometries and an augmented 'crossing disks'+SS73 scenario. See § 4.1.

(iv) We found the variability of trough A is best explained by a 'crossing disk' traversing a SS73 disk at velocities between $10,000 < v$ (km s^{-1}) $< 18,000$. This model and velocity range allow us to predict trough A will disappear between $350 < t$ (days) $< 1,500$ after our last observation (GEM3). See § 4.1.

(v) Trough B is best explained by a flow-tube that has recently moved into the line of sight, travelling in the velocity range $8,000 < v$ (km s^{-1}) $< 56,000$. In this scenario, we have no constraint on how far a flow-tube extends, and thus cannot predict when trough B will disappear. See § 4.1.

(vi) Given some simple, conservative assumptions in a transverse velocity model, we constrained the distance from the black hole to the absorbing gas responsible for trough A $r_C \leqslant 186 \pm 75$ $R_{Sch} = 0.04 \pm 0.02$ pc given $v_{trans} > 10,000$ km s^{-1} and for trough B we contrain the distance to be $r_C \leqslant 350 \pm 140$ $R_{Sch} = 0.07 \pm 0.03$ pc for $v_{trans} > 8,000$ km s^{-1}. See § 4.1.1.

(vii) If we assume changes to the ionization parameter is the reason for the variability observed, the absorber responsible for trough A either has 724 cm^{-3} $\leqslant$ $n_{e,A} \leqslant$ 3.62 $\times$ $10^4(r_{equal,A}/r)^2$ cm^{-3} and is between $r_{equal,A} \leqslant r \leqslant 7r_{equal,A}$, or is at $r <$ 2.00 kpc with no constraint on the density. Similarly, the absorber that caused the emergence of trough B is either constrained by 1540 cm^{-3} $\leqslant n_{e,B} \leqslant 7.70\times10^4(r_{equal,B}/r)^2$ cm^{-3} and $r_{equal,B} \leqslant r \leqslant 7r_{equal,B}$, or is at $r_{equal} \geqslant$ 1.37 kpc, or

[7] This is for our assumed SED from Dunn et al. 2010, $U_H = Q_H/4\pi n_H c$, with $Q_H = 6.08\times10^{56}$ hydrogen-ionizing photons s^{-1} and $n_H = 0.82n_e$.

is at $r < 1.37$ kpc with no constraint on the density. See § 4.2.1.

Given the results above, we cannot rule out bulk motion or ionization changes as models of BAL variability. More observations of J0230 will, however, allow us to test if our predictions of how the troughs will vary in the future are accurate.

6 ACKNOWLEDGMENTS

We thank the referee for a thorough and helpful review. PBH and JAR are supported by NSERC. NFA would like to acknowledge financial support from TUBITAK (115F037). WNB would like to thank NSF grant AST-1516784.

Based on observations for Program IDs GN-2013B-Q-59, GN-2013B-Q-39, and GS-2013B-Q-21 obtained at the Gemini Observatory (processed using the Gemini IRAF package), which is operated by the Association of Universities for Research in Astronomy, Inc., under a cooperative agreement with the NSF on behalf of the Gemini partnership: the National Science Foundation (United States), the National Research Council (Canada), CONICYT (Chile), the Australian Research Council (Australia), Ministério da Ciência, Tecnologia e Inovação (Brazil) and Ministerio de Ciencia, Tecnología e Innovación Productiva (Argentina).

The authors wish to recognize and acknowledge the very significant cultural role and reverence that the summit of Mauna Kea has always had within the indigenous Hawaiian community. We are most fortunate to have the opportunity to conduct observations from this mountain.

Funding for SDSS-III has been provided by the Alfred P. Sloan Foundation, the Participating Institutions, the National Science Foundation, and the U.S. Department of Energy Office of Science. The SDSS-III web site is http://www.sdss3.org/.

SDSS-III is managed by the Astrophysical Research Consortium for the Participating Institutions of the SDSS-III Collaboration including the University of Arizona, the Brazilian Participation Group, Brookhaven National Laboratory, Carnegie Mellon University, University of Florida, the French Participation Group, the German Participation Group, Harvard University, the Instituto de Astrofisica de Canarias, the Michigan State/Notre Dame/JINA Participation Group, Johns Hopkins University, Lawrence Berkeley National Laboratory, Max Planck Institute for Astrophysics, Max Planck Institute for Extraterrestrial Physics, New Mexico State University, New York University, Ohio State University, Pennsylvania State University, University of Portsmouth, Princeton University, the Spanish Participation Group, University of Tokyo, University of Utah, Vanderbilt University, University of Virginia, University of Washington, and Yale University.

REFERENCES

Allen, J. T., Hewett, P. C., Maddox, N., Richards, G. T., & Belokurov, V. 2011, Mon. Not. R. Astron. Soc. , 410, 860

Arav, N., Borguet, B., Chamberlain, C., Edmonds, D., & Danforth, C. 2013, Mon. Not. R. Astron. Soc. , 436, 3286

Arav, N., Chamberlain, C., Kriss, G. A., Kaastra, J. S., Cappi, M., Mehdipour, M., Petrucci, P.-O., Steenbrugge, K. C., Behar, E., Bianchi, S., Boissay, R., Branduardi-Raymont, G., Costantini, E., Ely, J. C., Ebrero, J., di Gesu, L., Harrison, F. A., Kaspi, S., Malzac, J., De Marco, B., Matt, G., Nandra, K. P., Paltani, S., Peterson, B. M., Pinto, C., Ponti, G., Pozo Nuñez, F., De Rosa, A., Seta, H., Ursini, F., de Vries, C. P., Walton, D. J., & Whewell, M. 2015, Astron. Astrophys. , 577, A37

Arav, N., Edmonds, D., Borguet, B., Kriss, G. A., Kaastra, J. S., Behar, E., Bianchi, S., Cappi, M., Costantini, E., Detmers, R. G., Ebrero, J., Mehdipour, M., Paltani, S., Petrucci, P. O., Pinto, C., Ponti, G., Steenbrugge, K. C., & de Vries, C. P. 2012, Astron. Astrophys. , 544, A33

Arav, N., Korista, K. T., de Kool, M., Junkkarinen, V. T., & Begelman, M. C. 1999, Astrophys. J. , 516, 27

Baskin, A., Laor, A., & Stern, J. 2014, Mon. Not. R. Astron. Soc. , 445, 3025

Blackburne, J. A., Pooley, D., Rappaport, S., & Schechter, P. L. 2011, Astrophys. J. , 729, 34

Capellupo, D. M., Hamann, F., Shields, J. C., Halpern, J. P., & Barlow, T. A. 2013, Mon. Not. R. Astron. Soc. , 429, 1872

Chamberlain, C., Arav, N., & Benn, C. 2015, Mon. Not. R. Astron. Soc. , 450, 1085

Chartas, G., Brandt, W. N., Gallagher, S. C., & Garmire, G. P. 2002, Astrophys. J. , 579, 169

Dawson, K. S., Schlegel, D. J., Ahn, C. P., Anderson, S. F., Aubourg, É., Bailey, S., Barkhouser, R. H., Bautista, J. E., Beifiori, A., Berlind, A. A., Bhardwaj, V., Bizyaev, D., Blake, C. H., Blanton, M. R., Blomqvist, M., Bolton, A. S., Borde, A., Bovy, J., Brandt, W. N., Brewington, H., Brinkmann, J., Brown, P. J., Brownstein, J. R., Bundy, K., Busca, N. G., Carithers, W., Carnero, A. R., Carr, M. A., Chen, Y., Comparat, J., Connolly, N., Cope, F., Croft, R. A. C., Cuesta, A. J., da Costa, L. N., Davenport, J. R. A., Delubac, T., de Putter, R., Dhital, S., Ealet, A., Ebelke, G. L., Eisenstein, D. J., Escoffier, S., Fan, X., Filiz Ak, N., Finley, H., Font-Ribera, A., Génova-Santos, R., Gunn, J. E., Guo, H., Haggard, D., Hall, P. B., Hamilton, J.-C., Harris, B., Harris, D. W., Ho, S., Hogg, D. W., Holder, D., Honscheid, K., Huehnerhoff, J., Jordan, B., Jordan, W. P., Kauffmann, G., Kazin, E. A., Kirkby, D., Klaene, M. A., Kneib, J.-P., Le Goff, J.-M., Lee, K.-G., Long, D. C., Loomis, C. P., Lundgren, B., Lupton, R. H., Maia, M. A. G., Makler, M., Malanushenko, E., Malanushenko, V., Mandelbaum, R., Manera, M., Maraston, C., Margala, D., Masters, K. L., McBride, C. K., McDonald, P., McGreer, I. D., McMahon, R. G., Mena, O., Miralda-Escudé, J., Montero-Dorta, A. D., Montesano, F., Muna, D., Myers, A. D., Naugle, T., Nichol, R. C., Noterdaeme, P., Nuza, S. E., Olmstead, M. D., Oravetz, A., Oravetz, D. J., Owen, R., Padmanabhan, N., Palanque-Delabrouille, N., Pan, K., Parejko, J. K., Pâris, I., Percival, W. J., Pérez-Fournon, I., Pérez-Ràfols, I., Petitjean, P., Pfaffenberger, R., Pforr, J.,

Pieri, M. M., Prada, F., Price-Whelan, A. M., Raddick, M. J., Rebolo, R., Rich, J., Richards, G. T., Rockosi, C. M., Roe, N. A., Ross, A. J., Ross, N. P., Rossi, G., Rubiño-Martin, J. A., Samushia, L., Sánchez, A. G., Sayres, C., Schmidt, S. J., Schneider, D. P., Scóccola, C. G., Seo, H.-J., Shelden, A., Sheldon, E., Shen, Y., Shu, Y., Slosar, A., Smee, S. A., Snedden, S. A., Stauffer, F., Steele, O., Strauss, M. A., Streblyanska, A., Suzuki, N., Swanson, M. E. C., Tal, T., Tanaka, M., Thomas, D., Tinker, J. L., Tojeiro, R., Tremonti, C. A., Vargas Magaña, M., Verde, L., Viel, M., Wake, D. A., Watson, M., Weaver, B. A., Weinberg, D. H., Weiner, B. J., West, A. A., White, M., Wood-Vasey, W. M., Yeche, C., Zehavi, I., Zhao, G.-B., & Zheng, Z. 2013, Astron. J. , 145, 10

Dere, K. P., Landi, E., Mason, H. E., Monsignori Fossi, B. C., & Young, P. R. 1997, Astron. Astrophys. Suppl. Ser. , 125, 149

Dexter, J. & Agol, E. 2011, Astrophys. J. Lett. , 727, L24

Dunn, J. P., Bautista, M., Arav, N., Moe, M., Korista, K., Costantini, E., Benn, C., Ellison, S., & Edmonds, D. 2010, Astrophys. J. , 709, 611

Edelson, R., Gelbord, J. M., Horne, K., McHardy, I. M., Peterson, B. M., Arévalo, P., Breeveld, A. A., De Rosa, G., Evans, P. A., Goad, M. R., Kriss, G. A., Brandt, W. N., Gehrels, N., Grupe, D., Kennea, J. A., Kochanek, C. S., Nousek, J. A., Papadakis, I., Siegel, M., Starkey, D., Uttley, P., Vaughan, S., Young, S., Barth, A. J., Bentz, M. C., Brewer, B. J., Crenshaw, D. M., Dalla Bontà, E., De Lorenzo-Cáceres, A., Denney, K. D., Dietrich, M., Ely, J., Fausnaugh, M. M., Grier, C. J., Hall, P. B., Kaastra, J., Kelly, B. C., Korista, K. T., Lira, P., Mathur, S., Netzer, H., Pancoast, A., Pei, L., Pogge, R. W., Schimoia, J. S., Treu, T., Vestergaard, M., Villforth, C., Yan, H., & Zu, Y. 2015, Astrophys. J. , 806, 129

Faucher-Giguère, C.-A., Quataert, E., & Murray, N. 2012, Mon. Not. R. Astron. Soc. , 420, 1347

Filiz Ak, N., Brandt, W. N., Hall, P. B., Schneider, D. P., Anderson, S. F., Gibson, R. R., Lundgren, B. F., Myers, A. D., Petitjean, P., Ross, N. P., Shen, Y., York, D. G., Bizyaev, D., Brinkmann, J., Malanushenko, E., Oravetz, D. J., Pan, K., Simmons, A. E., & Weaver, B. A. 2012, Astrophys. J. , 757, 114

Filiz Ak, N., Brandt, W. N., Hall, P. B., Schneider, D. P., Anderson, S. F., Hamann, F., Lundgren, B. F., Myers, A. D., Pâris, I., Petitjean, P., Ross, N. P., Shen, Y., & York, D. 2013, Astrophys. J. , 777, 168

Foltz, C. B., Wilkes, B., Weymann, R., & Turnshek, D. 1983, PASP, 95, 341

Gibson, R. R., Brandt, W. N., Schneider, D. P., & Gallagher, S. C. 2008, Astrophys. J. , 675, 985

Grier, C. J., Hall, P. B., Brandt, W. N., Trump, J. R., Shen, Y., Vivek, M., Filiz Ak, N., Chen, Y., Dawson, K. S., Denney, K. D., Green, P. J., Jiang, L., Kochanek, C. S., McGreer, I. D., Pâris, I., Peterson, B. M., Schneider, D. P., Tao, C., Wood-Vasey, W. M., Bizyaev, D., Ge, J., Kinemuchi, K., Oravetz, D., Pan, K., & Simmons, A. 2015, Astrophys. J. , 806, 111

Hall, P. B., Anderson, S. F., Strauss, M. A., York, D. G., Richards, G. T., Fan, X., Knapp, G. R., Schneider, D. P., Vanden Berk, D. E., Geballe, T. R., Bauer, A. E., Becker, R. H., Davis, M., Rix, H.-W., Nichol, R. C., Bahcall, N. A., Brinkmann, J., Brunner, R., Connolly, A. J., Csabai, I., Doi, M., Fukugita, M., Gunn, J. E., Haiman, Z., Harvanek, M., Heckman, T. M., Hennessy, G. S., Inada, N., Ivezić, Ž., Johnston, D., Kleinman, S., Krolik, J. H., Krzesinski, J., Kunszt, P. Z., Lamb, D. Q., Long, D. C., Lupton, R. H., Miknaitis, G., Munn, J. A., Narayanan, V. K., Neilsen, E., Newman, P. R., Nitta, A., Okamura, S., Pentericci, L., Pier, J. R., Schlegel, D. J., Snedden, S., Szalay, A. S., Thakar, A. R., Tsvetanov, Z., White, R. L., & Zheng, W. 2002, Astrophys. J. Suppl. Ser. , 141, 267

Hall, P. B., Anosov, K., White, R. L., Brandt, W. N., Gregg, M. D., Gibson, R. R., Becker, R. H., & Schneider, D. P. 2011, Mon. Not. R. Astron. Soc. , 411, 2653

Hall, P. B., Noordeh, E. S., Chajet, L. S., Weiss, E., & Nixon, C. J. 2013, ArXiv e-prints

Hall, P. B., Sadavoy, S. I., Hutsemekers, D., Everett, J. E., & Rafiee, A. 2007, Astrophys. J. , 665, 174

Hamann, F., Barlow, T. A., Beaver, E. A., Burbidge, E. M., Cohen, R. D., Junkkarinen, V., & Lyons, R. 1995, Astrophys. J. , 443, 606

Hamann, F., Barlow, T. A., Junkkarinen, V., & Burbidge, E. M. 1997, Astrophys. J. , 478, 80

Hamann, F., Kaplan, K. F., Rodríguez Hidalgo, P., Prochaska, J. X., & Herbert-Fort, S. 2008, Mon. Not. R. Astron. Soc. , 391, L39

He, Z.-C., Bian, W.-H., Ge, X., & Jiang, X.-L. 2015, Mon. Not. R. Astron. Soc. , 454, 3962

Ivezić, Ž., Menou, K., Knapp, G. R., Strauss, M. A., Lupton, R. H., Vanden Berk, D. E., Richards, G. T., Tremonti, C., Weinstein, M. A., Anderson, S., Bahcall, N. A., Becker, R. H., Bernardi, M., Blanton, M., Eisenstein, D., Fan, X., Finkbeiner, D., Finlator, K., Frieman, J., Gunn, J. E., Hall, P. B., Kim, R. S. J., Kinkhabwala, A., Narayanan, V. K., Rockosi, C. M., Schlegel, D., Schneider, D. P., Strateva, I., SubbaRao, M., Thakar, A. R., Voges, W., White, R. L., Yanny, B., Brinkmann, J., Doi, M., Fukugita, M., Hennessy, G. S., Munn, J. A., Nichol, R. C., & York, D. G. 2002, Astron. J. , 124, 2364

Jannuzi, B. T., Hartig, G. F., Kirhakos, S., Sargent, W. L. W., Turnshek, D. A., Weymann, R. J., Bahcall, J. N., Bergeron, J., Boksenberg, A., Savage, B. D., Schneider, D. P., & Wolfe, A. M. 1996, ApJL, 470, L11

Jiménez-Vicente, J., Mediavilla, E., Muñoz, J. A., & Kochanek, C. S. 2012, Astrophys. J. , 751, 106

Kallman, T. R. & McCray, R. 1982, Astrophys. J. Suppl. Ser. , 50, 263

Kaspi, S., Brandt, W. N., George, I. M., Netzer, H., Crenshaw, D. M., Gabel, J. R., Hamann, F. W., Kaiser, M. E., Koratkar, A., Kraemer, S. B., Kriss, G. A., Mathur, S., Mushotzky, R. F., Nandra, K., Peterson, B. M., Shields, J. C., Turner, T. J., & Zheng, W. 2002, Astrophys. J. , 574, 643

Krolik, J. H. 1999, Active galactic nuclei : from the central black hole to the galactic environment

Landi, E., Young, P. R., Dere, K. P., Del Zanna, G., & Mason, H. E. 2013, Astrophys. J. , 763, 86

Laor, A. & Brandt, W. N. 2002, Astrophys. J. , 569, 641

Leighly, K. M., Halpern, J. P., Jenkins, E. B., & Casebeer, D. 2007, Astrophys. J. Suppl. Ser. , 173, 1

Leighly, K. M., Hamann, F., Casebeer, D. A., & Grupe, D. 2009, Astrophys. J. , 701, 176

Leighly, K. M., Terndrup, D. M., Baron, E., Lucy, A. B.,

Dietrich, M., & Gallagher, S. C. 2014, Astrophys. J. , 788, 123
Luo, B., Brandt, W. N., Hall, P. B., Wu, J., Anderson, S. F., Garmire, G. P., Gibson, R. R., Plotkin, R. M., Richards, G. T., Schneider, D. P., Shemmer, O., & Shen, Y. 2015, Astrophys. J. , 805, 122
MacLeod, C. L., Ivezić, Ž., Kochanek, C. S., Kozłowski, S., Kelly, B., Bullock, E., Kimball, A., Sesar, B., Westman, D., Brooks, K., Gibson, R., Becker, A. C., & de Vries, W. H. 2010, Astrophys. J. , 721, 1014
McDowell, J. C., Canizares, C., Elvis, M., Lawrence, A., Markoff, S., Mathur, S., & Wilkes, B. J. 1995, Astrophys. J. , 450, 585
Moe, M., Arav, N., Bautista, M. A., & Korista, K. T. 2009, Astrophys. J. , 706, 525
Morgan, C. W., Kochanek, C. S., Morgan, N. D., & Falco, E. E. 2010, Astrophys. J. , 712, 1129
Murray, N. & Chiang, J. 1997, ApJ, 474, 91
Murray, N., Chiang, J., Grossman, S. A., & Voit, G. M. 1995, Astrophys. J. , 451, 498
Muzahid, S., Srianand, R., Charlton, J., & Eracleous, M. 2015, ArXiv e-prints
Narayanan, D., Hamann, F., Barlow, T., Burbidge, E. M., Cohen, R. D., Junkkarinen, V., & Lyons, R. 2004, Astrophys. J. , 601, 715
Ostriker, J. P., Choi, E., Ciotti, L., Novak, G. S., & Proga, D. 2010, Astrophys. J. , 722, 642
Pâris, I., Petitjean, P., Aubourg, É., Bailey, S., Ross, N. P., Myers, A. D., Strauss, M. A., Anderson, S. F., Arnau, E., Bautista, J., Bizyaev, D., Bolton, A. S., Bovy, J., Brandt, W. N., Brewington, H., Browstein, J. R., Busca, N., Capellupo, D., Carithers, W., Croft, R. A. C., Dawson, K., Delubac, T., Ebelke, G., Eisenstein, D. J., Engelke, P., Fan, X., Filiz Ak, N., Finley, H., Font-Ribera, A., Ge, J., Gibson, R. R., Hall, P. B., Hamann, F., Hennawi, J. F., Ho, S., Hogg, D. W., Ivezić, Ž., Jiang, L., Kimball, A. E., Kirkby, D., Kirkpatrick, J. A., Lee, K.-G., Le Goff, J.-M., Lundgren, B., MacLeod, C. L., Malanushenko, E., Malanushenko, V., Maraston, C., McGreer, I. D., McMahon, R. G., Miralda-Escudé, J., Muna, D., Noterdaeme, P., Oravetz, D., Palanque-Delabrouille, N., Pan, K., Perez-Fournon, I., Pieri, M. M., Richards, G. T., Rollinde, E., Sheldon, E. S., Schlegel, D. J., Schneider, D. P., Slosar, A., Shelden, A., Shen, Y., Simmons, A., Snedden, S., Suzuki, N., Tinker, J., Viel, M., Weaver, B. A., Weinberg, D. H., White, M., Wood-Vasey, W. M., & Yèche, C. 2012, Astron. Astrophys. , 548, A66
Pâris, I., Petitjean, P., Aubourg, É., Ross, N. P., Myers, A. D., Streblyanska, A., Bailey, S., Hall, P. B., Strauss, M. A., Anderson, S. F., Bizyaev, D., Borde, A., Brinkmann, J., Bovy, J., Brandt, W. N., Brewington, H., Brownstein, J. R., Cook, B. A., Ebelke, G., Fan, X., Filiz Ak, N., Finley, H., Font-Ribera, A., Ge, J., Hamann, F., Ho, S., Jiang, L., Kinemuchi, K., Malanushenko, E., Malanushenko, V., Marchante, M., McGreer, I. D., McMahon, R. G., Miralda-Escudé, J., Muna, D., Noterdaeme, P., Oravetz, D., Palanque-Delabrouille, N., Pan, K., Perez-Fournon, I., Pieri, M., Riffel, R., Schlegel, D. J., Schneider, D. P., Simmons, A., Viel, M., Weaver, B. A., Wood-Vasey, W. M., Yèche, C., & York, D. G. 2014, Astron. Astrophys. , 563, A54
Pietrini, P. & Krolik, J. H. 1995, Astrophys. J. , 447, 526
Plotkin, R. M., Anderson, S. F., Brandt, W. N., Diamond-Stanic, A. M., Fan, X., Hall, P. B., Kimball, A. E., Richmond, M. W., Schneider, D. P., Shemmer, O., Voges, W., York, D. G., Bahcall, N. A., Snedden, S., Bizyaev, D., Brewington, H., Malanushenko, V., Malanushenko, E., Oravetz, D., Pan, K., & Simmons, A. 2010, Astron. J. , 139, 390
Pounds, K. A., King, A. R., Page, K. L., & O'Brien, P. T. 2003, Mon. Not. R. Astron. Soc. , 346, 1025
Rafiee, A. & Hall, P. B. 2011, Astrophys. J. Suppl. Ser. , 194, 42
Richards, G. T., Lacy, M., Storrie-Lombardi, L. J., Hall, P. B., Gallagher, S. C., Hines, D. C., Fan, X., Papovich, C., Vanden Berk, D. E., Trammell, G. B., Schneider, D. P., Vestergaard, M., York, D. G., Jester, S., Anderson, S. F., Budavári, T., & Szalay, A. S. 2006, ApJS, 166, 470
Rodríguez Hidalgo, P., Hamann, F., & Hall, P. 2011, MNRAS, 411, 247
Rogerson, J. A., Hall, P. B., Snedden, S. A., Brotherton, M. S., & Anderson, S. F. 2011, New Astron. , 16, 128
Schneider, D. P., Hall, P. B., Richards, G. T., Strauss, M. A., Vanden Berk, D. E., Anderson, S. F., Brandt, W. N., Fan, X., Jester, S., Gray, J., Gunn, J. E., SubbaRao, M. U., Thakar, A. R., Stoughton, C., Szalay, A. S., Yanny, B., York, D. G., Bahcall, N. A., Barentine, J., Blanton, M. R., Brewington, H., Brinkmann, J., Brunner, R. J., Castander, F. J., Csabai, I., Frieman, J. A., Fukugita, M., Harvanek, M., Hogg, D. W., Ivezić, Ž., Kent, S. M., Kleinman, S. J., Knapp, G. R., Kron, R. G., Krzesiński, J., Long, D. C., Lupton, R. H., Nitta, A., Pier, J. R., Saxe, D. H., Shen, Y., Snedden, S. A., Weinberg, D. H., & Wu, J. 2007, Astron. J. , 134, 102
Schneider, D. P., Richards, G. T., Hall, P. B., Strauss, M. A., Anderson, S. F., Boroson, T. A., Ross, N. P., Shen, Y., Brandt, W. N., Fan, X., Inada, N., Jester, S., Knapp, G. R., Krawczyk, C. M., Thakar, A. R., Vanden Berk, D. E., Voges, W., Yanny, B., York, D. G., Bahcall, N. A., Bizyaev, D., Blanton, M. R., Brewington, H., Brinkmann, J., Eisenstein, D., Frieman, J. A., Fukugita, M., Gray, J., Gunn, J. E., Hibon, P., Ivezić, Ž., Kent, S. M., Kron, R. G., Lee, M. G., Lupton, R. H., Malanushenko, E., Malanushenko, V., Oravetz, D., Pan, K., Pier, J. R., Price, III, T. N., Saxe, D. H., Schlegel, D. J., Simmons, A., Snedden, S. A., SubbaRao, M. U., Szalay, A. S., & Weinberg, D. H. 2010, Astron. J. , 139, 2360
Shakura, N. I. & Sunyaev, R. A. 1973, Astron. Astrophys. , 24, 337
Trump, J. R., Hall, P. B., Reichard, T. A., Richards, G. T., Schneider, D. P., Vanden Berk, D. E., Knapp, G. R., Anderson, S. F., Fan, X., Brinkman, J., Kleinman, S. J., & Nitta, A. 2006, Astrophys. J. Suppl. Ser. , 165, 1
Vanden Berk, D. E., Richards, G. T., Bauer, A., Strauss, M. A., Schneider, D. P., Heckman, T. M., York, D. G., Hall, P. B., Fan, X., Knapp, G. R., Anderson, S. F., Annis, J., Bahcall, N. A., Bernardi, M., Briggs, J. W., Brinkmann, J., Brunner, R., Burles, S., Carey, L., Castander, F. J., Connolly, A. J., Crocker, J. H., Csabai, I., Doi, M., Finkbeiner, D., Friedman, S., Frieman, J. A., Fukugita, M., Gunn, J. E., Hennessy, G. S., Ivezić, Ž.,

Kent, S., Kunszt, P. Z., Lamb, D. Q., Leger, R. F., Long, D. C., Loveday, J., Lupton, R. H., Meiksin, A., Merelli, A., Munn, J. A., Newberg, H. J., Newcomb, M., Nichol, R. C., Owen, R., Pier, J. R., Pope, A., Rockosi, C. M., Schlegel, D. J., Siegmund, W. A., Smee, S., Snir, Y., Stoughton, C., Stubbs, C., SubbaRao, M., Szalay, A. S., Szokoly, G. P., Tremonti, C., Uomoto, A., Waddell, P., Yanny, B., & Zheng, W. 2001, Astron. J. , 122, 549

Wang, T., Yang, C., Wang, H., & Ferland, G. 2015, Astrophys. J. , 814, 150

Weymann, R. J., Morris, S. L., Foltz, C. B., & Hewett, P. C. 1991, Astrophys. J. , 373, 23

York, D. G., Adelman, J., & Anderson, Jr., J. E. e. a. 2000, Astron. J. , 120, 1579

Zoghbi, A., Miller, J. M., Walton, D. J., Harrison, F. A., Fabian, A. C., Reynolds, C. S., Boggs, S. E., Christensen, F. E., Craig, W., Hailey, C. J., Stern, D., & Zhang, W. W. 2015, Astrophys. J. Lett. , 799, L24